Editors' Suggestion

Spin-charge interplay in the diluted magnetic semiconductor Na(Zn,Mn)Sb studied by multiprobe measurements and simulations

Guoqiang Zhao,[1,2,3,*,†] Xiang Li,[1,*] Shuang Yu,[2] Hui Chen,[2] Yong Hu,[2,4] Yipeng Cai,[3,5] Shengli Guo,[6,7] Bo Gu,[1,8,‡] Fanlong Ning,[3,6,7] Kenji M. Kojima,[5] Zheng Deng,[2,8] Yuqing Xing,[2] Hong-Jun Gao,[2,8] Xingjiang Zhou,[2] Gang Su,[1,9] S. Maekawa,[1,10,11] Changqing Jin,[2,8] and Yasutomo J. Uemura[3,§]

[1]*Kavli Institute for Theoretical Sciences (KITS), University of Chinese Academy of Sciences, Beijing 101408, China*
[2]*Beijing National Laboratory for Condensed Matter Physics, and Institute of Physics, Chinese Academy of Sciences, Beijing 100190, China*
[3]*Department of Physics, Columbia University, New York, New York 10027, USA*
[4]*School of Physics, Chongqing University, Chongqing 400044, China*
[5]*TRIUMF, Vancouver, British Columbia, V6T 2A3 Canada*
[6]*School of Physics, Zhejiang University, Hangzhou 310027, China*
[7]*Collaborative Innovation Center of Advanced Microstructures, Nanjing University, Nanjing 210093, China*
[8]*School of Physics, University of Chinese Academy of Sciences, Beijing 101408, China*
[9]*Institute of Theoretical Physics, Chinese Academy of Sciences, Beijing 100190, China*
[10]*RIKEN Center for Emergent Matter Science (CEMS), Wako 315-0198, Japan*
[11]*Advanced Science Research Center (ASRC), Japan Atomic Energy Agency, Tokai 319-1195, Japan*

(Received 7 December 2024; revised 29 May 2025; accepted 16 June 2025; published 4 August 2025)

Diluted magnetic semiconductor (DMS) systems have been extensively studied in recent decades. DMSs provides a platform where charge transport and magnetic ordering phenomena exhibit unique interplays, together with possible applications to spin-dependent electronics (spintronics) devices. Initial development of ferromagnetic (FM) DMS systems centered around III-V semiconductors doped with dilute transition metals, such as (Ga,Mn)As, obtained by co-doping of spin and charge. More recently, independent spin and charge doping was first achieved in Li(Zn,Mn)As, a DMS system based on I-II-V semiconductor, with charge doping via variable Li concentrations and spin doping via iso-valent (Zn,Mn) substitutions. Although more than 30 new DMS systems with independent spin and charge doping have been synthesized since then, the main research emphasis has been put on development and characterization of systems with higher FM Curie temperature (T_C) and different crystal structures suitable for possible formation of heterostructure devices. This article focuses on a new DMS material Na(Zn,Mn)Sb, which exhibits a spin glass (SG) ordering, together with metal-insulator transition (MIT) and colossal negative magnetoresistance (CMR) as a function of independent spin and charge doping and application of external magnetic fields. MIT and CMR phenomena are elucidated by magneto transport, magnetization, angle resolved photoemission spectroscopy (ARPES), and scanning tunneling microscopy (STM) measurements, and by band calculations which demonstrate development and disappearance of energy gap. Magnetic order and dynamic spin fluctuations are probed with muon spin relaxation (μSR) and magnetization, and the results for Na(Zn,Mn)Sb are compared to those from FM DMS systems Li(Zn,Mn)As, Li(Zn,Mn)P, and Li(Zn,Mn,Cu)As. First-principles calculations are performed for Na(Zn,Mn)Sb, (Ga,Mn)As and Li(Zn,Mn)P to highlight the roles of charge and spin doping on exchange interactions mediated by nearest neighbor super-exchange coupling and oscillatory Ruderman-Kittel-Kasuya-Yosida (RKKY) coupling via conduction electrons. These studies reveal (1) MIT and CMR of Na(Zn,Mn)Sb manifest as a response to spin configurations as spin-driven transport phenomena; (2) a dynamic critical behavior is observed in SG transition of Na(Zn,Mn)Sb, in contrast to more first-order-like magnetic evolutions in other FM DMS systems; (3) charge doping supports FM coupling additive to direct AFM exchange interaction between nearest-neighbor Mn pairs; and (4) a widely different coercive fields seen in different families of FM and SG DMS systems can be explained by geometrical frustration of AFM interaction in underlying lattice for Mn spin network.

DOI: 10.1103/myxg-tt85

I. INTRODUCTION

Diluted magnetic semiconductor (DMS) systems represent a vibrant field that examines the complex interactions between magnetism and transport properties of various systems and dimensions [1–15] with a broad spectrum of phenomena [16–24]. DMS systems can be classified into two principal categories based on their magnetic ordering properties: spin glasses (SGs) and diluted ferromagnetic semiconductors

*These authors contributed equally to this work.
†Contact author: g.q.zhao@iphy.ac.cn
‡Contact author: gubo@ucas.ac.cn
§Contact author: yu2@columbia.edu

(DFSs). Various DMS systems demonstrate notable characteristics, including the metal-insulator transition (MIT), colossal negative magnetoresistance (CMR), and carrier-mediated ferromagnetism [11,25].

Among them, (Ga,Mn)As and related material systems [7,11,26–28] have functioned as a testbed for investigating novel concepts and properties of DMSs system over the past several decades since their initial discovery [29] and the subsequent efforts to achieve elevated Curie temperatures (T_C) [30]. The manganese (Mn) atoms in (Ga,Mn)As exhibit 4–5 Bohr magnetons of spin each, with the effective ferromagnetic (FM) interaction being facilitated by a Ruderman-Kittel-Kasuya-Yosida (RKKY)-like interaction between the Mn atoms and hole carriers. This phenomenon can be attributed to the low carrier density and the fact that the RKKY-like oscillation length scale significantly exceeds the interatomic distance between neighboring Mn atoms. The theoretical framework has been further advanced into the "*p-d* Zener model" [31,32], while an alternative perspective, referred to as the "Mn impurity-band model" [33], has also been proposed to explain the mechanisms underlying FM coupling. Debates among these models still continue [7,25,34]. However, the overall behavior of spin and charge interplay in (Ga,Mn)As is rather simple: the semiconductor to metal transition and the paramagnet to ferromagnet transition occur at nearly the same concentration of ∼4% Mn, and the FM T_C increases with increasing (Ga,Mn) substitutions, until the direct antiferromagnetic (AFM) exchange interaction between nearest neighbor (n.n.) Mn atoms start to suppress the FM tendency in the region of modest to high Mn concentrations.

In (Ga,Mn)As, trivalent Ga^{3+} is substituted by divalent Mn^{2+}. This implies simultaneous doping of spins and holes, which leads to the following difficulties. (1) Theoretically, it is difficult to distinguish the role played by spin doping with that by charge doping, even with the use of high-resolution analytical tools [35]. (2) This "hetero-valent" doping severely limits solubility and necessitate the use of low-temperature molecular beam epitaxy techniques to obtain metastable films. Bulk specimens cannot be generated, and thin film specimens often face problems arising from homogeneity and/or air sensitivity, such as different properties and conflicting results between pristine and annealed specimens [36,37]. Due to the unavailability of bulk specimens, detailed neutron scattering studies for detection of magnetic structure [7,25,26], and spin dynamics cannot be performed, although useful planar-averaged depth profiles of magnetic and nuclear scattering can be extracted from specular neutron reflection [38]. We shall call these systems the first-generation DMS systems.

In 2007, Masek, Jungwirth, and co-workers proposed [39] that one could overcome such difficulties of the Mn-doped III-V semiconductors by starting from a I-II-V semiconductor, such as LiZnAs, and making isovalent (Zn,Mn) substitutions for spin doping, while using excess Li for charge doping. Subsequently, Li(Zn,Mn)As was synthesized as a bulk material [2], and shown to exhibit FM properties similar to (Ga,Mn)As. This discovery of a new FM DMS system led to the development of series of Mn-based FM DMS systems with independent spin and charge doping, as reported in both experimental [3,4,40–96] and theoretical [97–111] studies. All these systems exhibit a FM phase for optimized spin and charge doping. Compared with (Ga,Mn)As and other DMS systems based on III-V semiconductors, these new DMS systems have the following advantages (i)–(iv). (i) A higher T_C ranging from 180 K [47] to 230 K [53] and up to 260 K [95] achieved in systems based on $BaZn_2As_2$ (BZA). There remains a possibility for further enhancement of T_C, as predicted by theoretical calculations [100,105,109]. (ii) They have potential for multilayer heterojunctions in spintronic devices [47,112–114], due primarily to the fact that the *p*-type (Ba, K)$(Zn, Mn)_2As_2$ [47,70] has a common crystal structure with the *n*-type DMSs $Ba(Zn, Co)_2As_2$ [77], antiferromagnet $BaMn_2As_2$ [115,116] and prototypical iron-based high-*Tc* superconductor $(Ba, K)Fe_2As_2$ [117]. (iii) Bulk and air-stable materials in single crystal are available [70,73], allowing access to various experimental techniques, such as angle-resolved photoemission spectroscopy (ARPES) [56], Andreev reflection [70], electronical transport [73], application of high pressure [75], and angle-dependent x-ray magnetic circular dichroism (XMCD) [86]. (iv) The distinct roles and effects of carriers and spins can possibly be separated through the independent manipulation of spin and charge doping [113,114]. We shall call these systems the second-generation DMS systems.

As the most recent family of DMSs with independent spin and charge doping, Na(Zn,Mn)Sb was synthesized in 2023 [1]. This system has several distinct properties as compared with FM DMS systems discussed above. The undoped compound NaZnSb is a metal, in contrast to semiconductors in the earlier FM DMS systems. In the optimally doped region, Na(Zn,Mn)Sb exhibits a spin glass (SG) phase rather than FM order. With spin and charge doping, this system exhibits semiconducting behavior in zero field, unlike the metallic behavior of the earlier FM DMSs. The semiconducting transport can be altered by the application of a high external field, which results in colossal negative magneto resistance (CMR). These features indicate that Na(Zn,Mn)Sb exhibits a new and unique interplay of transport (charge) and magnetism (spin) which is significantly different from those in the FM DMS systems. We shall call these systems the third-generation DMS systems.

In this paper, we elucidate the charge-spin interplay of Na(Zn,Mn)Sb systems by performing experimental measurements with several different probes including resistivity, magnetic susceptibility, magnetization, ARPES, scanning tunneling microscopy (STM), and muon spin relaxation (μSR), and by combining the results with band calculations and first-principle simulations of exchange interactions. The evolution with charge and spin doping will be compared with the behavior in FM DMS systems to highlight novel features of MIT and CMR and magnetic critical behaviors in Na(Zn,Mn)Sb. Finally, we will compare all the above-mentioned FM and SG DMS systems and show that the widely different values of the coercive field may be related to geometrical frustration of the AFM interactions in the underlying lattice of Mn networks. Following this introductory section, we will present a description of experimental and simulation methods in Sec. II, MIT and CMR results in Sec. III, μSR results in Sec. IV, and simulation of exchange interactions in Sec. V. Section VI, with a discussion and conclusions, will present three main conclusions and a notable observation from the results of the present study.

II. METHODS

Samples of Li(Zn,Mn)As [2], Na(Zn,Mn)Sb [1], Li(Zn,Cu,Mn)As [4], and Li(Zn,Mn)P [3,40,42] were synthesized utilizing both the conventional solid-state reaction method and the self-flux method [70]. The electronic transport properties were characterized by using a conventional four-probe method within a Physical Property Measurement System (PPMS, Quantum Design), with silver paint applied as an electrical contact on the sample. High-resolution ARPES measurements were conducted using a laboratory-based system at the Institute of Physics, Chinese Academy of Sciences (IoPCAS), which was equipped with a Scienta Omicron DA30 electron energy analyzer. The light source employed was a Scienta Omicron helium discharge lamp, providing a photon energy of 21.2 eV [118]. The energy resolution was established at 10–20 meV for Fermi surface mapping and band structure measurements, accompanied by an angular resolution of approximately 0.3 degrees. All measurements were performed under ultrahigh vacuum conditions, maintaining a base pressure of less than 5×10^{-11} Torr throughout the experiments, conducted at a temperature of 20 K, where SG ordering formation occurs for cleaved single crystal specimen $Na_{1.09}(Zn_{0.88}Mn_{0.12})Sb$. The samples utilized in the experiments were cleaved *in situ* at a temperature of 80 K and subsequently transferred to a STM head. The experiments were conducted within an ultrahigh vacuum environment (1×10^{-10} mbar) and at ultra-low temperatures (40 mK), utilizing a system capable of generating a magnetic field of 9-2-2 T. All scanning parameters, including setpoint voltage and current, for the STM topographic images are detailed in the figure captions. Unless otherwise specified, the differential conductance (dI/dV) spectra were obtained using a standard lock-in amplifier operating at a modulation frequency of 973.1 Hz. A nonmagnetic tungsten tip was produced through electrochemical etching and was calibrated on a clean Au (111) surface, which was prepared by subjecting it to multiple cycles of argon ion sputtering followed by annealing at 500 °C.

The μSR spectra of the $Li_{1.15}(Zn_{0.9}Mn_{0.1})P$ sample were measured under zero-field (ZF) and transverse-field (TF) conditions using the General Purpose Surface-Muon Instrument (GPS) at the Paul Scherrer Institute (PSI) in Villigen, Switzerland. The remaining μSR spectra for the samples $Li_{1.04}(Zn_{0.9}Mn_{0.1})P$, Li(Zn,Mn)As, Li(Zn,Cu,Mn)As, and Na(Zn,Mn)Sb, which exhibit varying doping levels, were obtained at TRIUMF in Vancouver, Canada. These measurements were conducted using the LAMPF spectrometer and dilution refrigerator (DR) under ZF, longitudinal field (LF), and TF conditions. The μSR analysis was conducted in the time domain using the MUSR-FIT software package [119], which is based on the ROOT framework developed at CERN for analyzing data in particle physics.

First-principles simulations were conducted utilizing the projector augmented wave (PAW) method [120] in conjunction with the Vienna *Ab Initio* Simulation Package (VASP) [121]. The electron exchange-correlation function selected for this study was the generalized gradient approximation (GGA), specifically utilizing the Perdew-Burke-Ernzerhof (PBE) formulation [122]. The GGA plus on-site Coulomb repulsion U (GGA+U) approach by Dudarev *et al.* was used to describe strongly localized Mn 3*d* orbitals [123]. The effective on-site Coulomb interaction parameter (U = 4 eV) was applied to Mn 3*d* orbitals. Lattice constants and atomic positions were fully relaxed until the maximum force acting on all atoms was less than 1×10^{-4} eV and the total energy was converged to 1×10^{-8} eV with the Gaussian smearing method. The kinetic energy cutoff of 500 eV was employed. The Brillouin zone was sampled with an 8×8×8 Monkhorst-Pack grid [124] for pristine NaZnSb and LiZnP, while 4×4×4 Monkhorst–Pack grid for 2×2×2 supercells of doped NaZnSb and LiZnP, and 6×6×6 Monkhorst-Pack grid for 2×2×2 supercells of (Ga,Mn)As and 4×4×2 Monkhorst-Pack grid for 2×2×3 supercells of (Ga,Mn)As. All doping configurations are generated by disorder code [125,126]. An 8×8×8 Monkhorst-Pack grid was utilized for the structural optimization of the unit cells of pristine NaMnSb and LiMnP. In contrast, a 4×8×4 Monkhorst-Pack grid was employed for the 2×1×2 supercells of NaMnSb, while a 4×4×4 Monkhorst-Pack grid was used for the 2×2×2 supercells of LiMnP. For the energy calculations of the elemental substances sodium (Na), zinc (Zn), manganese (Mn), and antimony (Sb), an 8×8×8 Monkhorst-Pack grid was also adopted.

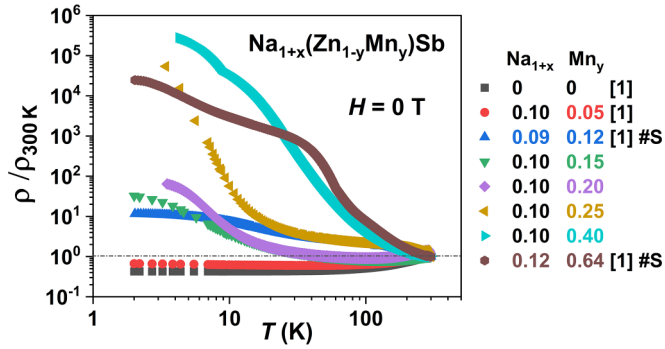

FIG. 1. Metal-insulator transition (MIT) in $Na_{1+x}(Zn_{1-y}Mn_y)Sb$. The normalized resistivity ratio $\rho/\rho_{300\,K}$ is plotted as a function of temperature. The MIT is observed as the Mn doping levels x increase while keeping the Na doping levels constant. The results are for polycrystalline samples, except for those on two single-crystal samples [1] with $x = 0.12$ and $y = 0.64$, and $x = 0.09$ and $y = 0.12$ donated as #S in the label.

III. METAL INSULATER TRANSITONS AND COLOSSAL MAGNETORESISTANCE: TRANSPORT, MAGNETIZATION, ARPES, AND STM MEASUREMENTS AND BAND CALCULATIONS

The MIT exhibit fluctuations and orderings in spin, charge, and orbital degrees of freedom near the transition point [127], and serves as a prominent and distinctive characteristic of strongly correlated electron systems, such as the Mott insulator [128] perovskite manganite [129], and DMSs [26], etc. Figure 1 demonstrates the MIT in $Na_{1+x}(Zn_{1-y}Mn_y)Sb$ material system. The parent compound NaZnSb has experimentally been confirmed to exhibit metallic properties [1], following the prediction made through first-principles tight-binding linear muffin-tin orbital calculations within the local density approximation (LDA) [refer to Fig. 5(a) below]. With

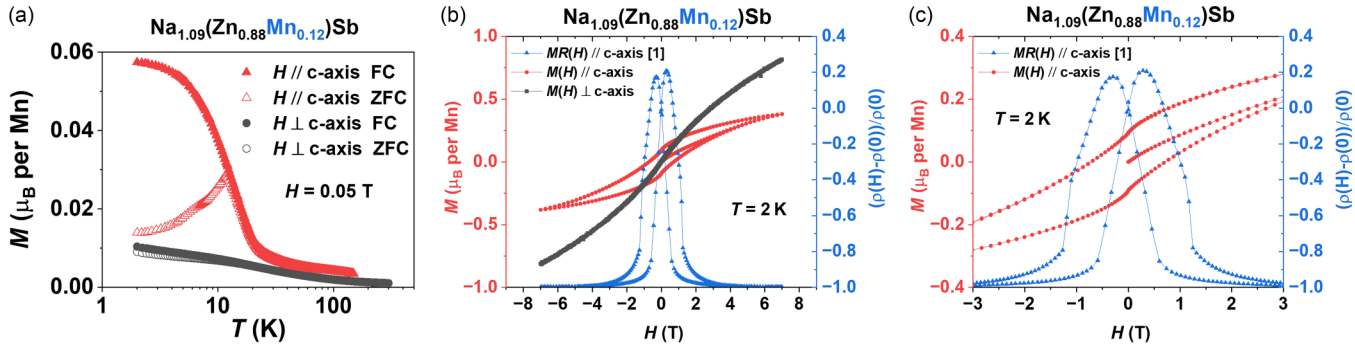

FIG. 2. Magnetization and MR in a single crystal specimen of $Na_{1.09}(Zn_{0.88}Mn_{0.12})Sb$. (a) The temperature dependence of the susceptibility with the external field $H = 0.05$ tesla (T) applied parallel to the c axis and the ab plane, respectively. (b) Magnetic hysteresis with H parallel to the c axis and the ab plane, respectively, and compared with the MR for H along the c axis at 2K. (c) Zoom in results of (b) with H parallel to the c axis.

an increase in magnetic manganese (Mn) concentration, an intriguing phenomenon arises: the normalized resistivity ratio ($\rho/\rho_{300\,K}$) exhibits a significant and rapid increase at low temperatures, especially below the spin freezing temperatures T_f, with values smaller than 20 K in all $Na_{1+x}(Zn_{1-y}Mn_y)Sb$ samples. The higher the Mn concentration, the more pronounced this upward trend becomes, accompanying a transition from Fermi liquid behavior to thermal activation. The Mn = 0.25 sample exhibits a resistivity approximately five orders of magnitude higher than that at room temperature, and nearly six orders of magnitude larger than that of the Mn = 0 and 0.05 samples at the lowest measured temperature. The alteration of the band structure and the magnetic structure can significantly influence resistivity.

ARPES, as a direct technique for observing the band structure, was employed to investigate single crystal $Na_{1.09}(Zn_{0.88}Mn_{0.12})Sb$ following preliminary magnetization and magnetoresistance (MR) characterization (Fig. 2). In conjunction with its resistivity under external fields [refer to Fig. 5(a) in Ref. [1]], we observed the following: (1) The T_f is approximately 12 K, with a notable increase in susceptibility commencing at around 20 K [Fig. 2(a)]. (2) The spin tends to freeze along the c axis of the crystal structure [Fig. 2(b)]. (3) Upon a gradual application of external fields, the alignment of spins can converge in a uniform direction, as demonstrated by the magnetic hysteresis loop at 2 K [Fig. 2(b)]. The alteration in spin structure referenced in point (3) shows a strong correlation with colossal magnetoresistance (CMR). The phenomenon of CMR will be elaborated upon in the subsequent section.

Initially, we will examine the band structure. The compound NaZnSb adopts a Cu_2Sb-type crystal structure (space group P4/nmm), which could be cleaved between the antimony (Sb) and sodium (Na) atomic layers [Fig. 3(a)]. Figure 3(b) exhibits the high-symmetry points in the Brillouin zones. Compared to NaZnSb, $Na_{1.09}(Zn_{0.88}Mn_{0.12})Sb$ exhibits a clear band gap smaller than 0.1 eV, as confirmed by direct measurements using the ARPES technique and shown in Figs. 3(c)–3(f). The constant-energy contours of NaZnSb at the binding energies (E_B) of 0 eV (Fermi level) (i) and 0.1 eV (ii) reveal a gapless feature, while the detailed band structure is depicted with cut #1 (i) and cut #2 (ii). The band structure calculations unequivocally rule out the possibility of a MIT caused by lattice distortion resulting from doping in the Na(Zn,Mn)Sb system (see Fig. 5 below).

The colossal negative magnetoresistance (CMR ≡ $[\rho(H)-\rho(0)]/\rho(0)$) [130], which refers to a much larger magnitude of negative magnetoresistance (MR) compared to conventional ferromagnetic metals, is an important topic in spintronics applications [9,26,112]. However, it is a complex subject due to material-specific complications and many-body interactions [25,121]. In the past decade, there has been a significant increase in research efforts on various types of CMR-related materials spinel [131,132], pyrochlore [133,134], cobaltite [135], SG [1], ferromagnetic semiconductor [136,137], half-Heusler compounds [138], and topological magnets [139,140]. Among these materials, perovskite manganite serves as a prototype example where concepts like magnetic polarons and magnetic phase separation have been developed [129,130,141,142]. However, the physics involved becomes highly intricate due to the interplay of numerous degrees of freedom, including spin, charge, orbital, and lattice dynamics, in addition to factors such as disorder and strong electron correlation. It is then desirable to study a relatively simple material to gain further insight into CMR. Just recently, a novel DMS Na(Zn,Mn)Sb [1] shows CMR in SG state, providing an excellent platform for studying its mechanism.

The doping evolution of CMR with respect to external fields in $Na_{1+x}(Zn_{1-y}Mn_y)Sb$ at the base temperature of 2 K is shown in Fig. 4(a). With an increasing doping concentration of Mn, the CMR initially increases and then decreases, with the highest value of 99.7% observed in the $Na_{1.1}(Zn_{0.75}Mn_{0.25})Sb$ sample. This value is comparable to that found in other magnetic materials such as europium monoxide [143], manganite [144,145], and chromium chalcogenides [132]. Moreover, the intrinsic nature is convincingly demonstrated by examining two doped single crystals, namely, $Na_{1.08}(Zn_{0.88}Mn_{0.12})Sb$ and $Na_{1.12}(Zn_{0.36}Mn_{0.64})Sb$, which effectively rule out any grain boundary effects observed in polycrystalline samples.

As early as 1934, de Haas and Van den Berg experimentally observed a minimum resistance in noble metals [146], which Kondo later explained using higher-order perturbation theory to determine the scattering rate between conduction electrons and magnetic impurities [147]. The "Kondo effect" is clearly demonstrated in the $Na_{1.1}(Zn_{0.95}Mn_{0.05})Sb$ sample without SG ordering, as shown by the logarithmic

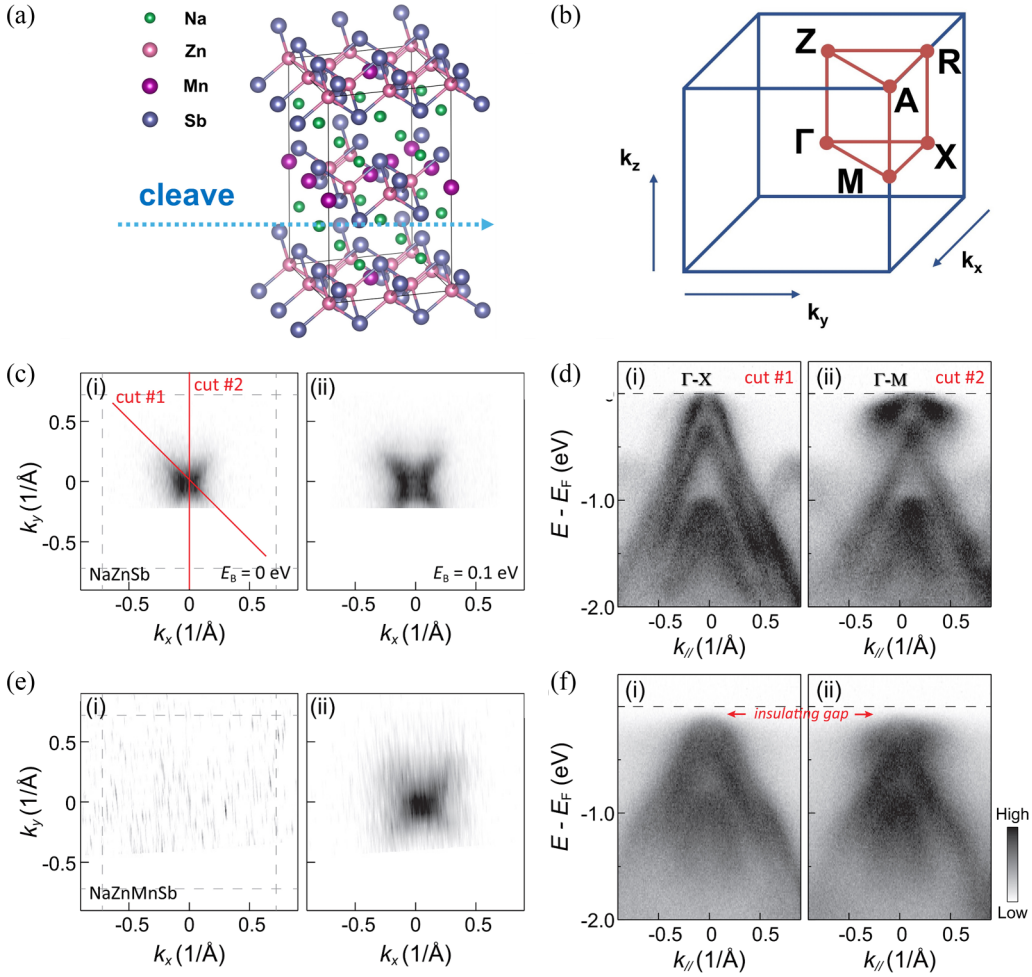

FIG. 3. ARPES results on single crystals of NaZnSb and $Na_{1.09}(Zn_{0.88}Mn_{0.12})Sb$. (a), (b) Crystal structure and momentum space configuration of $Na_{1+x}(Zn_{1-y}Mn_y)Sb$, with high-symmetry points indicated. The arrow in (a) indicates that the cleavage occurs between the Sb and Na atomic layers, producing two kinds of (001) surfaces with either As- or Na-terminated atomic layers. (c) Constant-energy contours of NaZnSb at the binding energies (EB) of 0 eV (Fermi level) (i) and 0.1 eV (ii). (d) The corresponding ARPES spectra of NaZnSb along two high-symmetry directions, cut no. 1 (i) and cut no. 2 (ii), as indicated by the red line in c(i). (e), (f) Same data as in (c) and (d), respectively, from $Na_{1.09}(Zn_{0.88}Mn_{0.12})Sb$. The red arrow in (f) highlights the insulating gap in the Mn-doped sample.

temperature-dependent increase in resistivity due to spin-flip scattering of magnetic impurities [Fig. 4(c)]. The same phenomena were also seen in SG CuMnBi alloys [148,149]. The resistivity of $Na_{1.1}(Zn_{1-y}Mn_y)Sb$ ($y = 0.15$ and 0.25) samples with SG ordering is significantly reduced by several orders of magnitude under external magnetic fields, leading to a remarkable increase in the magnetoresistance ratio $\rho(0)/\rho(H)$ [Fig. 4(b)]. This increase exceeds three orders of magnitude at the lowest measured temperature in the Mn = 0.25 SG sample. Extrapolating this trend to 2 K suggests an even more astounding magnetoresistance ratio approaching five orders of magnitude [Fig. 4(b)].

The observed CMR effects strongly correlate with the magnetic hysteresis loop observed at 2 K in both single crystal $Na_{1.09}(Zn_{0.88}Mn_{0.12})Sb$ [Fig. 2(b)] and $Na_{1.12}(Zn_{0.36}Mn_{0.64})Sb$ [refer to Figs. 2(c) and 5(d) in Ref. [1]]. The magnetization DC susceptibility measurements in $Na_{1.1}(Zn_{0.75}Mn_{0.25})Sb$ with a polycrystalline state under several selected external fields also demonstrate consistency with the CMR. The modification of spin structure caused by external fields can contribute to the occurrence of CMR phenomena. Specifically, as the temperature decreases, all spins tend to align themselves into specific orientations to minimize energy and form a metastable phase upon crossing the critical temperature point T_f. This metastable state can be perturbed by external fields that gradually realign the spin orientation as the field strength incrementally increases from 0 to 7 T. The scattering effects reach their minimum when all spins align in a single direction resembling a quasi-FM state, provided the external field is sufficiently strong, leading to the manifestation of CMR. The electronic structures of $Na(Zn_{1-y}Mn_y)Sb$ (Fig. 5) were calculated by using first-principles methods. This analysis serves to further validate that the alteration of the spin structure, resulting from Mn doping in an AFM configuration, also induces the colossal CMR phenomenon. The energy with a FM ground state magnetic structure [Figs. 5(f)–5(h)] is observed to be greater than that with an antiferromagnetic (AFM) magnetic structure [Figs. 5(b)–5(d)], under the same doping levels.

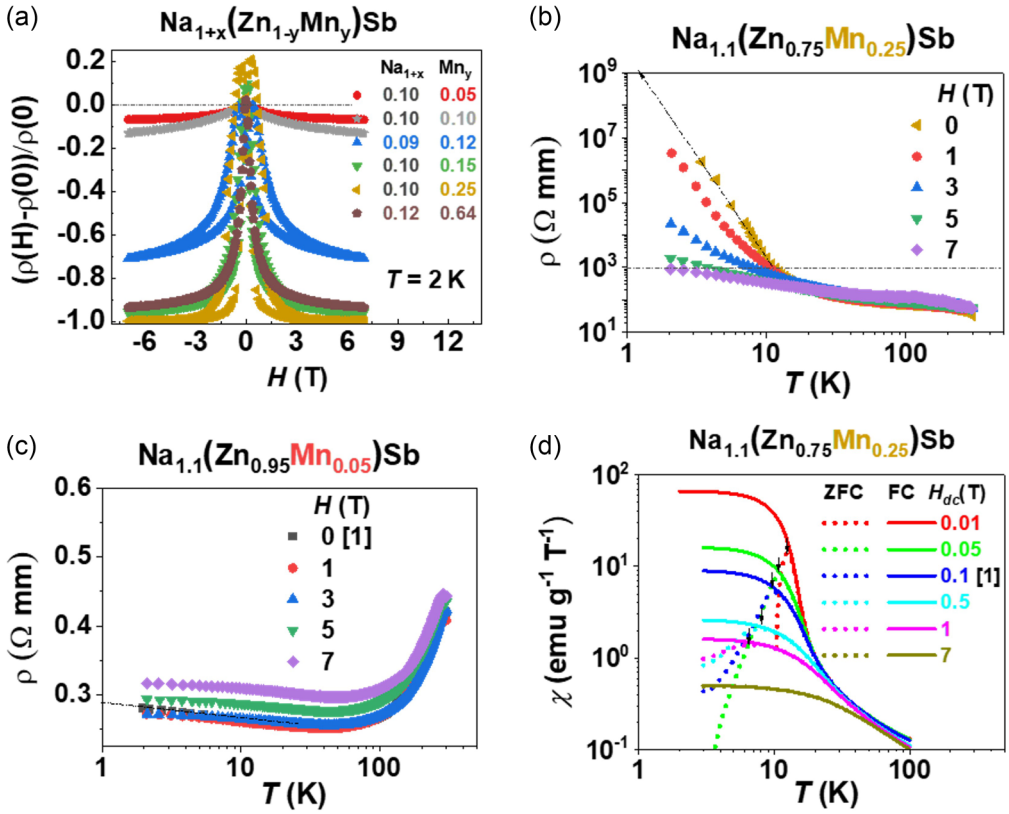

FIG. 4. The colossal negative magnetoresistance effects. (a) Magnetic-field dependence of the colossal negative magnetoresistance CMR $\equiv [\rho(\mathrm{H}) - \rho(0)]/\rho(0)$ in $Na_{1+x}(Zn_{1-y}Mn_y)Sb$ in various doping levels at $T = 2$ K. The specimens of Mn = 0.12 and 0.64 are single crystals [1], while other specimens are polycrystals. (b), (c) The resistivity $\rho(T)$ versus temperature at several selected external fields in $Na_{1.1}(Zn_{0.75}Mn_{0.25})Sb$ and $Na_{1.1}(Zn_{0.95}Mn_{0.05})Sb$. (d) Temperature dependence of the dc susceptibility in this specimen in selected external fields ranging from 0.01 T, 0.05 T, 0.1 T, 0.2 T, 1 T, up to 7 T.

The scanning tunneling microscopy/spectroscopy (STM) technique was used independently to investigate the atomic and electronic structure of $Na_{1.12}(Zn_{0.36}Mn_{0.64})Sb$ single crystal (Fig. 6). The weak bonding between neighboring Na layers leads to the formation of Na terminated surfaces after cleaving of the sample [Fig. 6(a)]. An atomically resolved STM image of the Na terminated surface of $Na_{1.12}(Zn_{0.36}Mn_{0.64})Sb$, reveals a distorted square lattice with dimensions $a = 4.3$ Å and $b = 4.0$ Å [Fig. 6(b)], compared to the calculated lattice with dimensions $a = b = 4.44$ Å. This distortion may be attributed to surface relaxation during the cleaving process. The dI/dV spectrum obtained at the Na terminated surface shows three peaks at the occupied states of about 250 mV, 360 mV, and 510 mV [Fig. 6(c)]. We apply external magnetic fields perpendicular to the surface Bz to study the magnetic response of the density of state. When Bz increases to 7 T, there is no significance for the density of states. This result provides clear elucidation that the CMR effect cannot be attributed to the band-structure change in the surface under external field [Fig. 6(d)]. Together with the band structure calculated above, we could claim that the increase of the density of states in the Fermi level is a bulk and intrinsic effect. The findings collectively indicate the contributions of the modification of the spin structure under external fields and its role in the CMR.

It is noteworthy that CMR effects have also been observed in (Ga,Mn)As systems. The substitution of Ga^{3+} with Mn^{2+} results in simultaneous charge and spin doping; however, researchers are actively pursuing modifications to the hole concentration through defect engineering via ion irradiation, all while maintaining a stable Mn concentration. Published studies [150,151] indicate that samples with a relatively high Mn concentration of 5%–6% can become insulating after hole compensation by defects. Furthermore, at sufficiently elevated Mn concentrations, if the samples are insulating, the colossal magnetoresistance can approach 100% [137], as demonstrated in Na(Zn, Mn)Sb.

IV. MAGNETIC PHASE TRANSITIONS IN Na(Zn,Mn)Sb AND RELATED FM DMS SYSTEMS

A. Spin glass phenomena and the previous μSR studies

In the previous sections, we have studied transport properties of Na(Zn,Mn)Sb to elucidate how the charge conduction properties are altered in response to the doping of charges and spins, and to the application of external magnetic fields. The conventional method for inducing ferromagnetism in nonmagnetic semiconductors involves doping with magnetic atoms, resulting in a transition from PM to FM, as seen in the (Ga,Mn)As system [152]. AFM and FM states can be achieved by attaining specific levels of magnetic atom doping, such as the Li(Zn,Mn)As [2,39,153] and (Ba, K)(Zn, Mn)$_2$As$_2$ [47,53,56,57,63,66,68,70,86,91,115,116,154–156], systems.

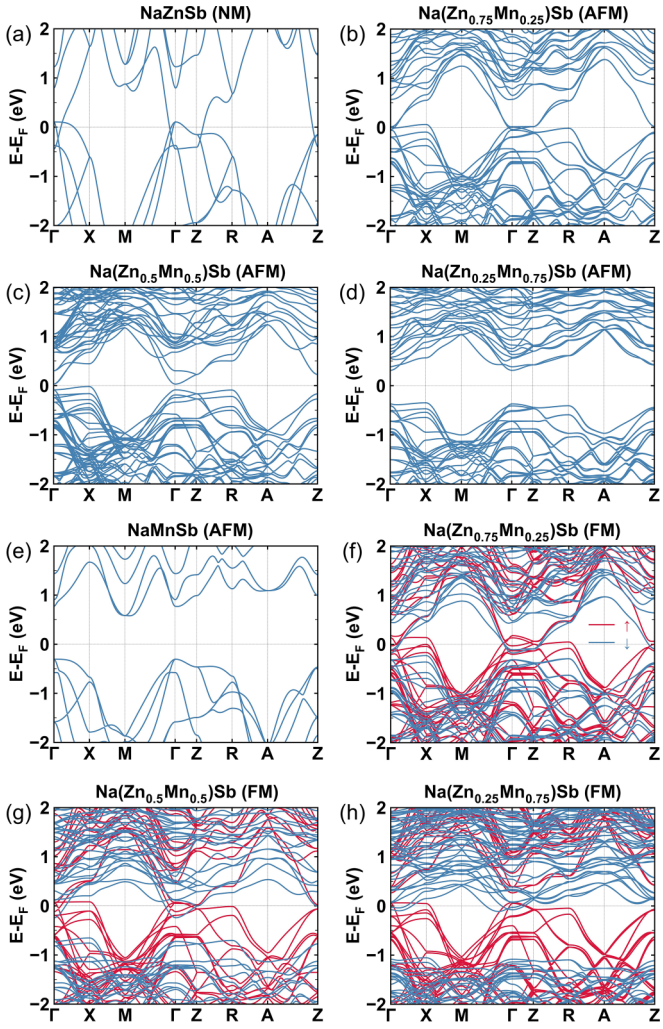

FIG. 5. First-principles calculation for the electronic structures of $Na(Zn_{1-y}Mn_y)Sb$. (a) NaZnSb. (b)–(d) $Na(Zn_{1-y}Mn_y)Sb$ ($y =$ 0.25, 0.5, and 0.75) with the AFM ground state magnetic structure. (e) NaMnSb. (f)–(h) $Na(Zn_{1-y}Mn_y)Sb$ ($y = 0.25$, 0.5, and 0.75) with the FM ground state magnetic structure. Note that the energy with FM magnetic structure is higher than that with the AFM magnetic structure.

Note that LiMnAs [153] and $(Ba, K)Mn_2As_2$ [115,116,154–156] are AFM systems with the antiferromagnetic coupling between nearest neighbor Mn pairs. As shown in the magnetic susceptibility and its field dependence (refer to Fig. 3 in Ref. [1]), Na(Zn,Mn)Sb exhibits properties characteristic of spin glasses (SGes). In this section, we shall study magnetic phases and spin fluctuations in Na(Zn,Mn)Sb and compare them with the results obtained in ferromagnetic DMS systems such as Li(Zn,Mn)As and Li(Zn,Mn)P, in order to understand how the SG state is obtained in a family of DMS systems.

In SG systems, which have been studied since the 1970s [157,158], spins are arranged with random directions in space without any periodicity and become "frozen" as a function of time, thereby violating the ergodicity principle. This stands in contrast to conventional FM and AFM where neighboring spins align parallel or antiparallel, as well as paramagnets which exhibit a spatially random spin pattern that fluctuates over time while maintaining ergodicity [159]. Consequently, numerous energy configurations arise from competing interactions between the spins. This situation leads to numerous energy configurations arising from competing interactions between the spins. The initial introduction within the framework of localization theory was provided by Anderson [160], motivated by the discovery of puzzling effects in AuFe and CuMn alloys by Cannella and Mydosh [161]. In these dilute alloy SGes, the competing and frustrating interactions originate from the spatially oscillating RKKY interaction among dilute magnetic moments of Mn or Fe due to Friedel oscillation of conduction electrons of the host material, Cu or Au. One of the most surprising features is the sharpness of the cusp of the ac-magnetic susceptibility observed in these dilute-alloy SG systems, despite the built-in randomness of spin locations and the resulting random directions of frozen spins below the cusp temperature. More recently, SG behaviors have also been observed in geometrically frustrated spin systems (GFSS) [162,163], which involve (at most) only a minimal degree of built-in randomness or broken translational symmetry in the locations of magnetic moments. Despite the accumulation of experimental and theoretical results, the fundamental nature of the ground state, energy landscapes, and spin dynamics of SG systems are still subject to extensive studies in various different systems [164]. The present work will explore the SG phenomena in a new platform of DMSs systems.

Here we will use the method of muon spin relaxation (μSR) to probe magnetic properties of Na(Zn,Mn)Sb and related systems. In the 1980s and early 1990s, μSR was applied to studies of CuMn [165–173], AuFe [174,175], AuMn [172,173], and AgMn [176–181], and the results revealed (1) development of static frozen component (order parameter) of Mn or Fe moments below the susceptibility-cusp temperature T_f; (2) a clear signature of critical slowing down of spin fluctuations with temperatures approaching T_f from above and below; and (3) the disappearance of dynamic spin relaxation at $T \to 0$. In a kagome lattice [182,183], pyrochlore [184–186] and many other GFSS systems, in contrast to the feature (3) in dilute alloy SGes, the muon spin relaxation rate $1/T_1$ often remains finite even at $T \to 0$, indicating some quantum spin dynamics persisting well below T_f. μSR was also applied to many DMS systems, such as (Ga.Mn)As [36], Li(Zn,Mn)As [2], and $(Ba, K)(Zn, Mn)_2As_2$ [47], elucidating static magnetic order together with the evolution of the volume fraction with static magnetism. These observations have been made possible by a superb sensitivity of μSR to magnetic order of spin systems even with random and/or dilute magnetic moments, and the unique ability of μSR to independently determine the size of the frozen local ordered moment and the volume fraction involving the static magnetic order [187]. Details of μSR methods can be found in books [188–190] and in reviews of time spectra expected in SGs [175] and various different magnetic systems [191].

B. μSR results in $Na_{1.1}(Zn_{0.75}Mn_{0.25})Sb$ and relevant DFSs systems

μSR measurements on $Na_{1.1}(Zn_{0.75}Mn_{0.25})Sb$ were performed at TRIUMF using sintered ceramic specimens. The irreversibility of DC magnetization shown in Fig. 4(d) and the frequency shifts in temperature in the ac susceptibility

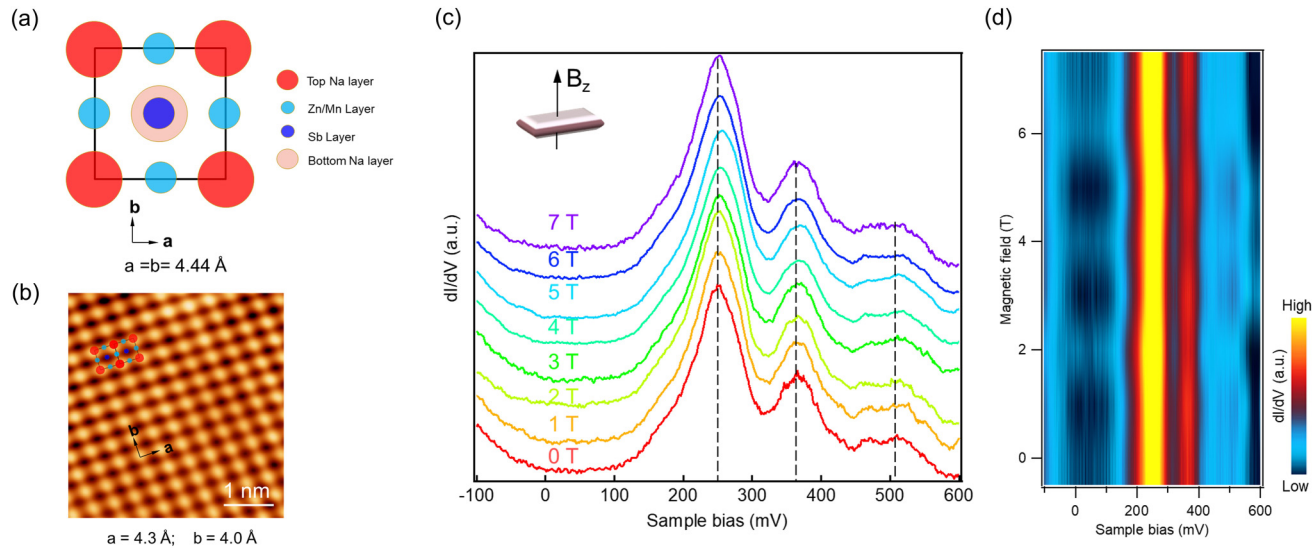

FIG. 6. STM results from single crystal $Na_{1.12}(Zn_{0.36}Mn_{0.64})Sb$. (a) Top view (*ab* plane) of a schematic model of $Na_{1.12}(Zn_{0.36}Mn_{0.64})Sb$, showing the atomic structure of top Na layer and underlying Zn/Mn, Sb and bottom Na layer with a unit cell of $a = b = 4.44$ Å. (b) Atomically resolved STM image of Na-terminated surface of Na(ZnMn)Sb, showing a lattice of $a = 4.3$ Å, $b = 4.0$ Å, taken with scanning parameters: Sample bias $V_s = 200$ mV, tunneling current: $I_t = 50$ pA. Waterfall (c) and intensity (d) plot of dI/dV spectra under the magnetic field perpendicular to the surface, showing no significant changes in the density of states with increasing magnetic field from 0 T to 7 T. STS parameters: Sample bias $V_s = -100$ mV, tunneling current: $I_t = 2$ nA.

measurements (refer to Fig. 3 in Ref. [1]) indicate the SG behavior of this system with the spin freezing temperature, $T_f = (12 \pm 1)$ K in zero external magnetic field. We took μSR data in zero field (ZF), weak-transverse field (wTF) of 24 G applied perpendicular to the direction of initial muon polarization, and several longitudinal fields (LFs) parallel to the initial polarization, with the positron counters located in forward/backward configuration in the non-spin-rotated mode, [refer to Fig. 1 in Ref. [175]). Typical time spectra of muon spin polarization for selected temperatures are shown in Fig. 7 with Fig. 7(a) for ZF, Fig. 7(b) for wTF, and Figs. 7(c) and 7(d) for LF μSR measurements.

Spin freezing below T_f would generate a significant random and static local field at the muon site, resulting in a fast depolarization of the "transverse component" (2/3 of total asymmetry in the case of powder/ceramic samples) in ZF-μSR, as shown in Fig. 7(a). The volume fraction of the region with strong static magnetism can be estimated via the amplitude of this transverse relaxation and precession component in ZF, as well as via the volume of the para- and nonmagnetic environment derived from the amplitude of oscillation component with applied field in the wTF measurements, shown in Fig. 7(b). In principle, μSR relaxation in ZF can be caused both by static random local field and the $1/T_1$ relaxation due to fluctuating dynamic local fields. These can be distinguished by the application of LF. The asymmetry lost by the static effect can be restored and decoupled by LF as shown in Fig. 7(c) for $T = 2$ K. The field required to cause this decoupling phenomenon scales with the magnitude of the static random local field which can also be determined by the initial fast decay rate of the asymmetry of transverse component in ZF. The dynamic $1/T_1$ relaxation, in contrast, does not exhibit significant change of relaxing asymmetry in LF, as shown in most of the data in Fig. 7(d) for LF = 500 G above T_f, although some field dependence can be seen in the relaxation rate which is partly due to the decoupling of the nuclear dipolar field above T_f. Application of LF 500 G also decouples the random static field from the frozen moments below T_f. With these principles, μSR time spectra can be analyzed using relaxation functions A(t), where fitting allows one to derive three essential parameters: (i) the magnitude of the static random local field, denoted as a_s, (ii) the volume fraction f_M of the region with static magnetism due to frozen ordered moments, and (iii) the dynamic spin relaxation rate $1/T_1$. The fitting functions used in the present study are given in the μSR analytical model and spectrum section of the Supplemental Material [192], with further explanations [192]. Although the nuclear dipolar field also causes static relaxation, its effect can be easily separated from those of static magnetic order and freezing, since the magnitude of nuclear dipolar field is smaller than those of frozen spins by more than two orders of magnitude in the systems studied in the present paper.

In Fig. 8(a) we present the results for the static random local field a_s and the volume fraction f_M with the static magnetism in $Na_{1.1}(Zn_{0.75}Mn_{0.25})Sb$ derived from the time spectra in ZF and wTF. We see a rather sharp change of these parameters at $T \sim T_f$, which indicates a sharp onset of the SG freezing. In ideal second-order (continuous) phase transitions, one would expect an increase of a_s scaling with the order parameter below T_f associated with a change of f_M as a step function at T_f. In first-order transitions involving phase s.eparation at T_f, the volume f_M often exhibits gradual changes while a_s often develops from finite values discontinuously [187,193,194]. The results in Fig. 8(a) suggest that the spin freezing in $Na_{1.1}(Zn_{0.75}Mn_{0.25})Sb$ exhibits features close to the second-order transition.

For the purpose of comparison, we also present μSR results on ferromagnetic DFS systems Li(Zn,Mn)As, Li(Zn,Mn)P, and Li(Zn,Cu,Mn)As in Figs. 8(b)–8(d)

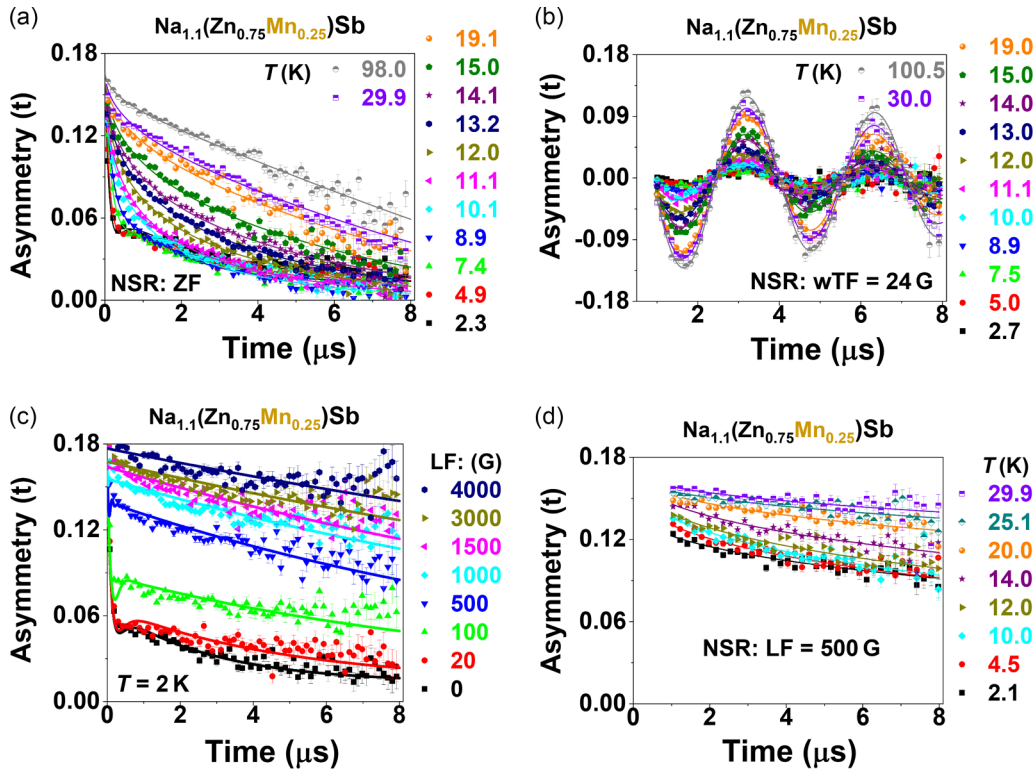

FIG. 7. μSR time spectra of $Na_{1.1}(Zn_{0.75}Mn_{0.25})Sb$ polycrystalline sample. (a) ZF. (b) wTF at 24 G. (c) LF at $T = 2$ K. (d) Temperature dependence at LF 500 G.

obtained with analyses using the same principles and fitting procedures applied to Na(Zn,Mn)Sb in Fig. 8(a). Magnetization and transport results on these systems have been published in [2–4,40]. A part of μSR results on these systems have also been published for $x = 0.1$, $y = 0.05$ of $Li_{1+x}(Zn_{1-y}, Mn_y)As$ [2], $x = 0.15$, $y = 0.1$

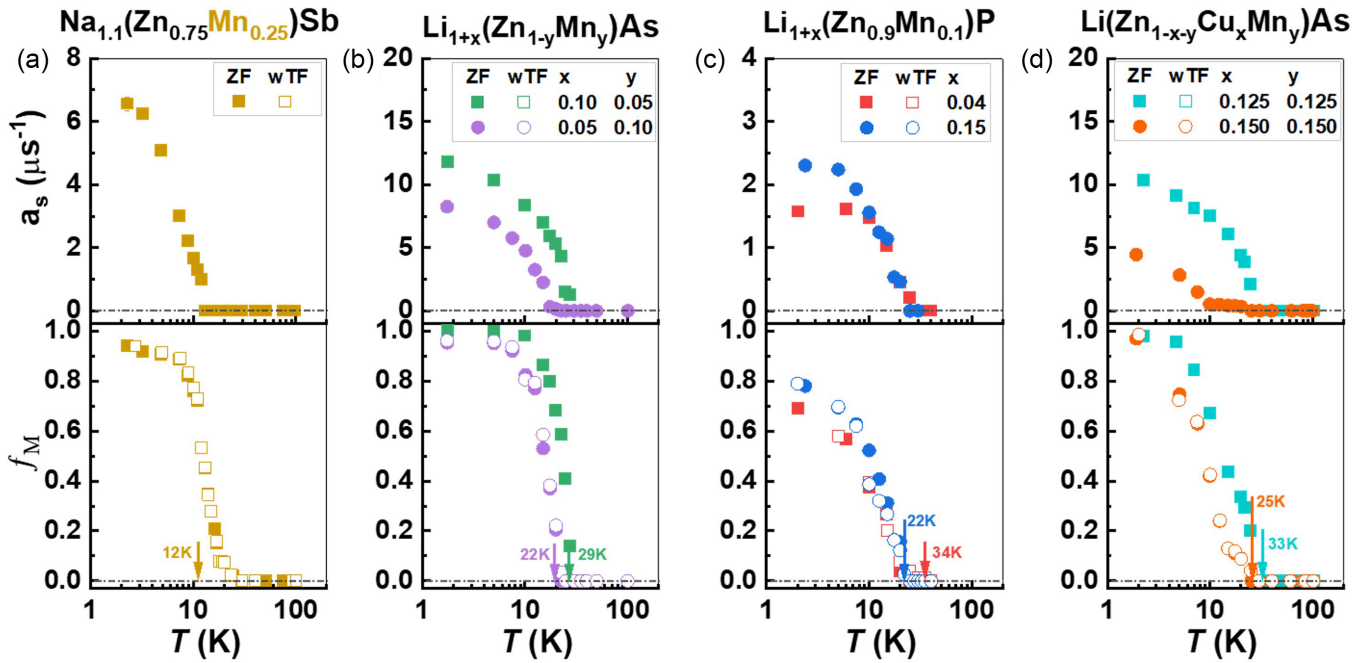

FIG. 8. Static ordered volume fraction f_M, and the amplitude of static random fields a_s versus temperature for SG and FM systems. (a) $Na_{1.1}(Zn_{0.75}Mn_{0.25})Sb$. (b) $Li_{1+x}(Zn_{1-y}Mn_y)As$. (c) $Li_{1+x}(Zn_{0.9}Mn_{0.1})P$. (d) $Li(Zn_{1-x}Cu_xMn_y)As$. Note that part of the results in (b)–(d) for $Li_{1.1}(Zn_{0.95}Mn_{0.05})As$ [2], $Li_{1.15}(Zn_{0.9}Mn_{0.1})P$ [3], and $Li(Zn_{0.75}Cu_{0.125}Mn_{0.125})As$ [4] have ever been reported. The positions of the arrows indicate the transition temperatures, and their corresponding values are illustrated, with each color representing a specific sample.

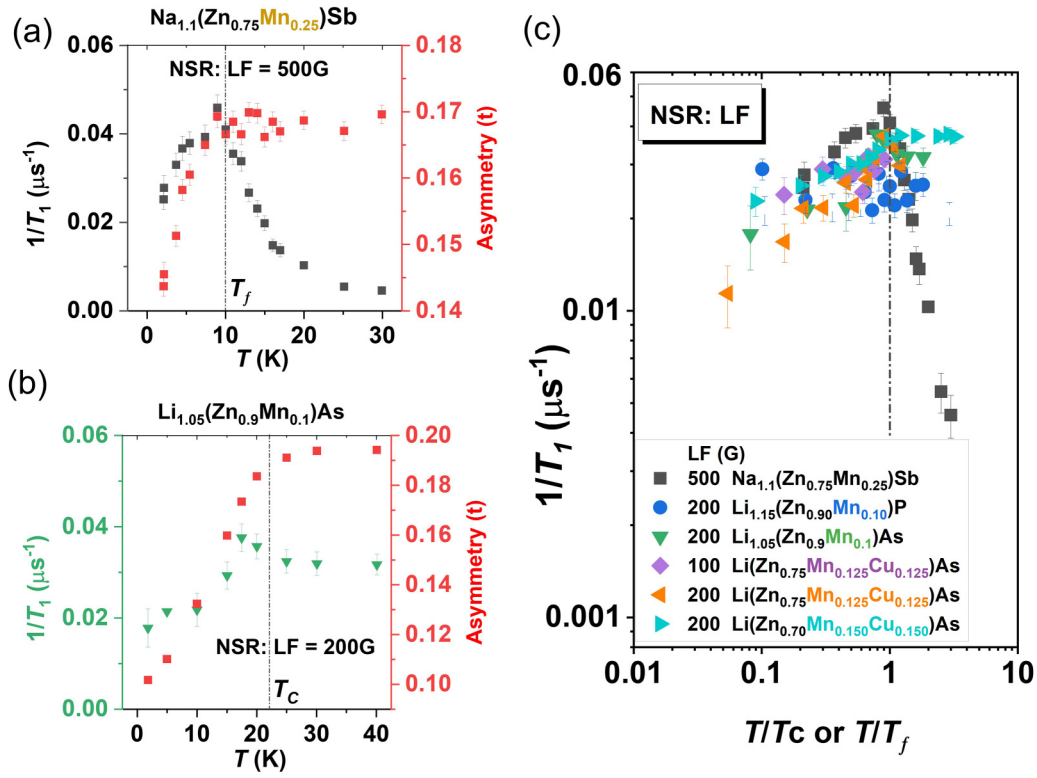

FIG. 9. $1/T_1$ versus normalized critical temperatures, retracted from longitudinal-field (LF)–μSR time spectra. Dynamic critical behavior appears around T_f for SG systems (a), but no dynamic critical behaviors for all the FM systems (b)–(c).

for $Li_{1+x}(Zn_{1-y}, Mn_y)P$ [3] and $x = 0.125$, $y = 0.125$ for $Li(Zn_{1-x-y}, Cu_x, Mn_y)As$ [4], while the results in other specimens of Figs. 8(b)–8(d) have been newly obtained and analyzed for the present paper. The new data were obtained at PSI for the wTF- and ZF-μSR of the $Li_{1.15}(Zn_{0.9}Mn_{0.1})P$ sample, and TRIUMF for the LF-μSR of $Li_{1.15}(Zn_{0.9}Mn_{0.1})P$ sample, all the configurations of $Na_{1.1}(Zn_{0.75}Mn_{0.25})Sb$, $Li_{1+x}(Zn_{1-y}, Mn_y)As$ ($x = 0$, $y = 0$; $x = 0.1$, $y = 0.03$; $x = 0.1$, $y = 0.05$; $x = 0.05$, $y = 0.1$), $Li_{1.04}(Zn_{0.9}Mn_{0.1})P$, and $Li(Zn_{1-x-y}, Cu_x, Mn_y)As$ ($x = 0.125$, $y = 0.125$; $x = 0.150$, $y = 0.150$). These ferromagnetic DMS systems exhibit results closer to the first-order transitions with gradual change of f_M around T_C and a gradual increase of f_M at low temperatures without saturation. Detailed analysis of the spectra was attached to Figs. S1–S3 in the Supplemental Material [192].

The differences between second- and first-order transitions also show up in the critical behavior of dynamic spin relaxation rate $1/T_1$. In Fig. 9 we compare the results of $1/T_1$ for these four different systems. In our reports [2–4] of μSR results for a part of the ferromagnetic DFS system in Figs. 8(b)–8(d), the previous analyses were performed without including the effect of the dynamic $1/T_1$ relaxation. For the present paper, we reanalyzed the μSR data in all the ferromagnetic DMS systems and present the results in Figs. 9(b) and 9(c). Detailed analysis of the spectra is attached to Figs. S4 and S5 [192]. A clear peaking of $1/T_1$ at T_f was observed in $Na_{1.1}(Zn_{0.75}Mn_{0.25})Sb$, as shown in Fig. 9(a), indicating critical slowing down of spin fluctuations at the spin freezing, similar to those observed in AuFe and CuMn [175]. In contrast, no peaking of $1/T_1$ was found in any of the DFS systems around their T_C's [Fig. 9(c)]. Both results of static order in Fig. 8(a) and dynamic critical behavior in Fig. 9(a) are consistent with a second-order phase transition in $Na_{1.1}(Zn_{0.75}Mn_{0.25})Sb$ at the SG spin freezing. Another notable feature is the tendency towards disappearance of $1/T_1$ and absence of persistent (quantum) spin dynamics at $T \to 0$ in $Na_{1.1}(Zn_{0.75}Mn_{0.25})Sb$. Thus the spin freezing in the DMS SG system $Na_{1.1}(Zn_{0.75}Mn_{0.25})Sb$ occurs in the manner quite similar to the case of dilute alloy SG systems [175].

C. Nearly linear scaling of the random static field amplitude a_s and the transition temperatures

In some of our previous reports on ferromagnetic DMS systems [2–4,36,41], we plotted the internal field parameter a_s against the transition temperature T_C, and demonstrated nearly linear correlations as shown in Fig. 10. This feature is similar to the relationship in dilute alloy spin glasses, where the exchange interaction is due to the RKKY interaction and internal field is due to dipolar field from the frozen moments. In the dilute limit, both interactions and fields decay with a $1/r^3$ dependence with the distance r from a magnetic moment. This leads to a_s and T_C both scaling linearly with the concentration c of Mn or Fe moments, and thus to the linear relationship between a_s and T_C with c as an implicit parameter. When plotted in Fig. 10, the results on $Na_{1.1}(Zn_{0.75}Mn_{0.25})Sb$ closely follow the trend of other DMS systems. This implies that the magnitude and spatial variation of the exchange interaction in the SG system are comparable to those in the ferromagnetic DMS systems. This feature will be discussed further in the next section, based on first-principle theoretical simulations.

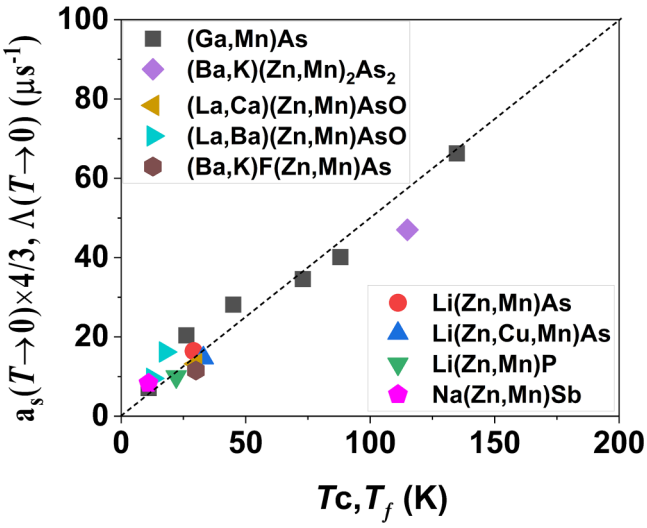

FIG. 10. Correlations between the μSR static internal field a_s ($T = 2$ K) and the transition Curie temperature T_C and spin freezing temperature T_f observed in various DMS systems, including $(Ga_{1-x}Mn_x)As$ ($x = 0.012$, 0.030, 0.034, and 0.070) [36], $(Ba_{0.8}K_{0.2})(Zn_{0.9}Mn_{0.1})_2As_2$ [47], $(La_{0.9}Ca_{0.1})(Zn_{0.9}Mn_{0.1})AsO$ [62], $(La_{0.95}Ba_{0.05})(Zn_{0.95}Mn_{0.05})AsO$ [41], $(Ba_{0.85}K_{0.15})F(Zn_{0.9}Mn_{0.1})As$ [59], $Li_{1.1}(Zn_{0.95}Mn_{0.05})As$ [2], $Li(Zn_{0.75}Cu_{0.125}Mn_{0.125})As$ [4], and $Li_{1.15}(Zn_{0.9}Mn_{0.1})P$ [3].

V. FIRST-PRINCIPLES CALCULATIONS OF EXCHANGE INTERACTIONS

To obtain further understandings of the origin of the contrasting SG and FM behaviors, we conducted first-principles simulations of exchange interactions in Na(Zn,Mn)Sb and Li(Zn,Mn)P as examples of systems showing, respectively, the SG and FM properties. As illustrated in Fig. 11(a), Li(Zn,Mn)P, (Ga,Mn)As, Li(Zn,Mn)As, and Li(Zn,Cu,Mn)As exhibit ferromagnetic properties while sharing the same cubic crystal structure (space group, F-43m), in contrast to layered tetragonal structures of NaMnSb and LiMnAs which display antiferromagnetic properties [195,196]. Without Mn, NaZnSb and LiZnP exhibit nonmagnetic behavior, but the crystal structure of NaZnSb is layered tetragonal, remaining to be the same as that of NaMnSb while LiZnP has a cubic structure. The excess Na or Li atoms in the antiferromagnetic material Na(Zn,Mn)Sb and Li(Zn,Mn)P are believed to substitute Zn sites, according to the formation energy calculations, thereby contributing to hole carrier doping. Our primary focus is on the Na(Zn,Mn)Sb system. A Heisenberg Hamiltonian is used to describe the magnetic system

$$H = E_0 + \Sigma_{\langle i,j\rangle} J_1 S_i \cdot S_j + \Sigma_{\langle\langle i,j\rangle\rangle} J_2 S_i \cdot S_j + \Sigma_{\langle\langle\langle i,j\rangle\rangle\rangle} J_3 S_i S_j + \Sigma_{\langle i,i'\rangle} J_\perp S_i S_{i'}, \quad (1)$$

where J_1, J_2, and J_3 represent intralayer couplings of the nearest, next-nearest, and third-nearest neighbors, respectively. Meanwhile, $J_\perp$ represents interlayer coupling. In Fig. 11(a), we show these couplings by choosing Mn atom "0" as the origin, while Mn atoms "1", "2", "3", and "⊥" pairing with "0", respectively with J_1, J_2, J_3, and $J_\perp$. In addition, E_0 denotes the energy independent of magnetism. The ferromagnetic coupling between two Mn impurities occurs when $J < 0$, while the antiferromagnetic coupling occurs when $J > 0$. The calculated results are presented in Table I.

The magnetic critical temperature is calculated by using the mean-field formula

$$T_{N/C}^{\mathrm{MFA}} = \frac{2}{3k_B} S(S+1) \left| \sum_i \sum_\alpha Z_i^\alpha P_\alpha J_i \right|, \quad (2)$$

where Z_i^α represents the coordination number of Mn impurities in one specific doping configuration, α for the given concentration, P_α denotes the probability of this particular doping configuration, and J_i with i = 1, 2, 3, ⊥ respectively. It should be noted that $S = 5/2$ corresponds to the spin of the Mn impurity arising from five local d orbits. The mean-field formula is expected to consistently overestimate the critical temperature [197,198], thus necessitating the adoption of a rescaling method for a more reliable estimation. For example, the

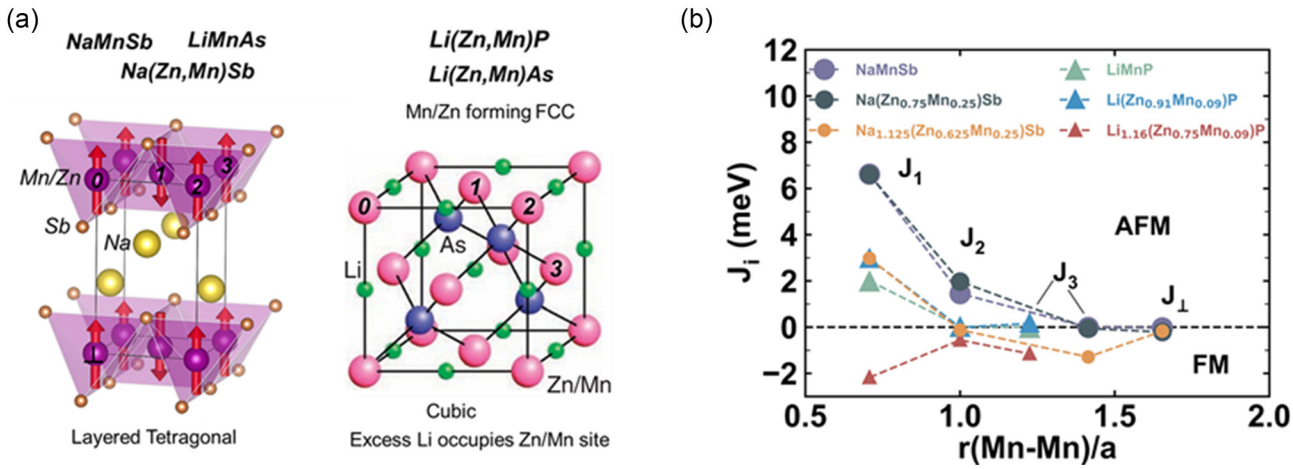

FIG. 11. Crystal structure and magnetic exchange couplings of Mn cations in $Na_{1+x}(Zn_{1-x-y}Mn_y)Sb$ and $Li_{1+x}(Zn_{1-x-y}Mn_y)P$. J_1, J_2, and J_3 stand for intralayer couplings of the nearest, the next-nearest, and the third-nearest neighbors, $J_\perp$ stands for interlayer coupling, which are marked by different colors in schematic (a) and calculated results from Table I are depicted in (b) where a is the lattice constant of NaMnSb or LiMnP.

TABLE I. First-principles exchange couplings of Mn impurities, mean-field critical temperatures (Néel temperature T_N^{MFA} and Curie temperature T_C^{MFA}), and rescaled critical temperatures (Néel temperature T_N, Curie temperature T_C and spin glass freezing temperature T_f) for (Ga,Mn)As, Na(Zn,Mn)Sb and Li(Zn,Mn)P systems. J_1, J_2, J_3, and $J_\perp$ are intralayer couplings of the nearest, next-nearest, third-nearest neighbors, and interlayer couplings respectively. Two Mn impurities are coupled ferromagnetically for conditions of $J < 0$ while antiferromagnetically for conditions of $J > 0$.

	First-principles calculations						Experiments	
Samples	J_1 (meV)	J_2 (meV)	J_3 (meV)	$J_\perp$ (meV)	T_N^{MFA} or T_C^{MFA} (K)	Rescaled T_N or T_C (K)	Samples	T_N, T_C, or T_f (K)
$(Ga_{0.94}Mn_{0.06})As$	−10.38	0.07	−1.14	–	379.9	$T_C = 104.8$	$(Ga_{0.948}Mn_{0.052})As$	$T_C = 132.0$[a]
$(Ga_{0.91}Mn_{0.09})As$	−10.04	0.65	−1.20	–	652.6	$T_C = 180.0$	$(Ga_{0.91}Mn_{0.09})As$	$T_C = 180.0$[a]
NaMnSb	6.62	1.45	−0.01	−0.03	2178.9	$T_N = 601.0$	NaMnSb	$T_N > 400$[b]
$Na(Zn_{0.75}Mn_{0.25})Sb$	6.60	1.97	−0.06	−0.21	422.3	$T_N = 116.5$	–	–
$Na_{1.125}(Zn_{0.625}Mn_{0.25})Sb$	2.98	−0.12	−1.29	−0.17	73.9	$T_N = 20.4$	$Na_{1.1}(Zn_{0.75}Mn_{0.25})Sb$	$T_f = 11.5$[c]
LiMnP	2.02	0.03	−0.01	–	1633.6	$T_N = 450.6$	–	–
$Li(Zn_{0.91}Mn_{0.09})P$	2.96	−0.01	0.16	–	175.7	$T_N = 48.5$	–	–
$Li_{1.16}(Zn_{0.75}Mn_{0.09})P$	−2.18	−0.56	−1.15	–	255.2	$T_C = 70.4$	$Li_{1.15}(Zn_{0.90}Mn_{0.10})P$	$T_C = 22$[d]
							$Li_{1.10}(Zn_{0.96}Mn_{0.04})P$	$T_C = 34$[e]

[a]Reference [199]; [b]Reference [196]; [c]Reference [1]; [d]Reference [3]; [e]Reference [40].

mean-field Curie temperature of (Ga, Mn)As with a 9% Mn concentration is calculated to be 652.6 K, which corresponds to the experimental value of 180 K for (Ga, Mn)As [199,200]. Based on this ratio of 3.63, we estimated the rescaled transition temperatures of other systems by dividing the mean-field calculation values by a factor 3.63. In Table I we show both of the unscaled and rescaled theoretical transition temperatures and compare them with the experimental values.

In Table I we first notice that the nearest neighbor (n.n.) AF coupling J_1 is very large for NaMnSb and $Na(Zn_{0.75}Mn_{0.25})Sb$. This large AF J_1 plays a crucial role in determining the antiferromagnetism of these materials.

NaMnSb shows strong AF behavior with both intralayer AF couplings including J_1 and J_2, resulting in Neel temperature above the room temperature. The magnetic ground state of NaMnSb is intralayer Neel-type antiferromagnetism with ultra weak interlayer ferromagnetic coupling, which indicates the intralayer coupling is essential for determining the magnetism of this layered material. $Na(Zn_{0.75}Mn_{0.25})Sb$ with Neel temperature of 116.5 K can be seen as the material with Mn cations substituted by Zn cations compared to pristine NaMnSb; i.e., with Mn spins diluted by nonmagnetic Zn leading to spin dilution without charge doping. J_1 and J_2 still remain antiferromagnetic, J_3 and $J_\perp$ remain ferromagnetic. With additional charge doping, in $Na_{1.125}(Zn_{0.625}Mn_{0.25})Sb$, J_1 becomes much lower, compared with charge-undoped $Na(Zn_{0.75}Mn_{0.25})Sb$ and NaMnSb, J_2 changes from antiferromagnetic to ferromagnetic, and the ferromagnetic coupling of J_3 is enhanced. This leads to competition between AF J_1 and FM J_2, J_3 and $J_\perp$ in $Na_{1.125}(Zn_{0.625}Mn_{0.25})Sb$, providing the theoretical estimate of AFM ground state with the rescaled Neel temperature of 20.4 K. In existing real material, this competition of AF and FM couplings results in the SG freezing with the freezing temperature $T_f = 11.5$ K [1]. This evolution highlights the role of charge doping to promote tendency towards ferromagnetism in Na(Zn,Mn)Sb, while the strong n.n. AF coupling in this system prevents FM ground state, leading to a unique SG state in existing materials as seen by experimental results of the present paper.

Following the same rationale, the *p*-type magnetic semiconductor $Li_{1+x}(Zn_{1-x-y}Mn_y)P$ is also investigated for comparative analysis. The $Li_{1+x}(Zn_{1-x-y}Mn_y)P$ compound exhibits paramagnetic behavior in the absence of excess Li atoms, and the interaction between two adjacent Mn impurities is antiferromagnetic [3,40,42]. The calculated exchange couplings reveal that J_1 and J_3 exhibit AF behavior, while J_2 displays weak ferromagnetism, as indicated in Table I, which is consistent with experimental observations. The rescaled Neel temperature of $Li(Zn_{0.91}Mn_{0.09})P$ is 48.5 K, and first-principles calculations reveal distinct magnetic behavior upon excess Li doping compared to $Na_{1+x}(Zn_{1-x-y}Mn_y)Sb$. Specifically, for $Li_{1.16}(Zn_{0.75}Mn_{0.09})P$ with *in situ* Li doping on the Zn site, all exchange couplings are mediated towards ferromagnetism without competition from antiferromagnetism, indicating an unlikely spin-glass behavior. The compound $Li_{1.16}(Zn_{0.75}Mn_{0.09})P$ exhibits ferromagnetic properties with a rescaled Curie temperature of 70.4 K, as shown in Table I, which is consistent with the relatively low experimental Curie temperature of 22 K observed for $Li_{1.15}(Zn_{0.9}Mn_{0.1})P$ [3]. The slight difference may be caused by the phase separation (only ∼80% static ordered volume fraction exits as shown in Fig. 9(b)). Together with Table I, Fig. 11(b) demonstrates the contrasting behaviors in exchange couplings between Na(Zn,Mn)Sb and Li(Zn,Mn)P systems.

VI. DISCUSSION AND CONCLUSIONS

In Table II we summarized the present results on Na(Zn,Mn)Sb with the evolution of charge and spin doping. For the purpose of comparison, we also listed the known results for Li(Zn,Mn)As in Table III, Li(Zn,Mn)P in Table IV, and (Ga,Mn)As in Table V. In this section, we discuss three main conclusions and observations from the present work.

A. Conclusion 1: MIT in Na(Zn,Mn)Sb driven by spin configurations

In Na(Zn,Mn)Sb, the spin configuration plays a decisive role in determining charge conduction. This is shown by

TABLE II. Summarized results for SG $Na_{1+x}(Zn_{1-y}Mn_y)Sb$ system. Note that the symbols for props, FIG, ct, semi-cond., and mag. are abbreviations for properties, figure, current work, semiconductor, and magnetization, respectively.

	NaZnSb		$Na_{1.09}(Zn_{0.88}Mn_{0.12})Sb$		$Na_{1.1}(Zn_{0.75}Mn_{0.25})Sb$		$Na_{1.12}(Zn_{0.36}Mn_{0.64})Sb$		NaMnSb	
Compound	props	FIG. [Ref]	props	FIG. [Ref]	props	FIG. [Ref]	props	FIG. [Ref]	props	FIG. [Ref]
Crystal	Layer tetragonal	3(a) [ct] and 1(a)[a]	Layer tetragonal	3(a) [ct] and 1(a)[a]	Layer tetragonal	3(a) [ct] and 1(a)[a]	Layer tetragonal	3(a) [ct] and 1(a)[a]	Layer tetragonal	4(a)[b]
Conductivity	Metal	4(a)[a]	Semi-Cond	5(a)[a]	Semi-Cond	1 [ct]	Semi-Cond	5(c)[a]	Semi-Cond	5(e) [ct] and 2(a)[b]
Mag. state	Non-mag.	–	SG from dc mag. *H*//c	2(a) [ct]	SG from ac mag.	3[a]	AFM	2(c)[a]	AFM	3(h)[b]
Trans. temp	–	–	∼12 K	2(a) [ct]	∼11.5 K	3[a]	∼11 K	2(c)[a]	T_N>400 K	3(c)[b]
STM	–	–	–	–	No field depend.	6 [ct]	–	–	–	–
CMR	–	–	−71.5% (7 T, 2 K)	4(a) [ct]	−99.7% (7 T, 2 K)	4(a) [ct]	−92.4% (7 T, 2 K)	4(a) [ct]	–	–
Band gap	No gap obtained from ARPES in Fig. 3(d) [ct]		Gap obtained from ARPES (<100 meV) in Fig. 3(f) [ct]		Gap obtained from resistivity in Fig. 1 [ct] (the value is not marked in the paper)		Gap obtained from resistivity in Fig. 5(a)[a] and Fig. 1 [ct] (the value is not marked in the paper)		Gap obtained from resistivity in Fig. 1(a)[b] (the value is not marked in the paper)	
	No gap obtained from GGA calculations in Fig. 5(a) [ct]		–		No gap for AFM and FM obtained from GGA calculations of $Na(Zn_{0.75}Mn_{0.25})Sb$ in Fig. 5(b) [ct] and Fig. 5(f) [ct]		Gap for AFM and no gap for FM obtained from GGA calculations of $Na(Zn_{0.50}Mn_{0.50})Sb$ and $Na(Zn_{0.25}Mn_{0.75})Sb$ (48.6 meV < gap < 659 meV) in Figs. 5(c) and 5(d) [ct] and Figs. 5(g) and 5(h) [ct]		Gap obtained from calculations (∼1250 meV, HSE06) in Fig. 6(c)[b] and (∼880 meV, GGA) in Fig. 5(e) [ct]	

[a]Reference [1]; [b]Reference [196].

TABLE III. Summarized results for DFSs $Li_{1+x}(Zn_{1-y}Mn_y)As$ systems. Note that the symbols for props, FIG, ct, semi-cond., and mag. are abbreviations for properties, figure, current work, semiconductor, and magnetization, respectively.

	LiZnAs		$Li_{1.1}ZnAs$		$Li_{1.1}(Zn_{0.95}Mn_{0.05})As$		LiMnAs	
Compound	props	FIG. [Ref]	props	FIG. [Ref]	props	FIG. [Ref]	props	FIG. or Tab. [Ref]
Crystal	Cubic	1(a)[a]	Cubic	1(a)[a]	Cubic	1(a)[a]	Layer tetragonal	1(b)[a]
Conductivity	Semi-Cond	2(a)[a]	Metal	2(a)[a]	Semi-Cond	2(b)[a]	Semi-Cond	3(c)[b]
Mag. state	Non-mag.	–	Non-mag.	–	FM from dc mag.	1(f) and 1(g)[a]	AFM	Table III[c]
Trans. temp	0	0	0	0	29 K	1(f)[a]	T_N=393 K	Table III[c]
CMR	–	–	–	–	–	–	27.9% (9 T, 2 K)	2(a)[f]
Band gap	Gap obtained from photoconductivity at 300 K (∼1250 meV) in Fig. 2(c)[d] and (∼1520 meV) in Fig. 4[g], or (∼1100 meV) obtained from resistivity in Fig. 4[h]		Gap obtained from resistivity in Fig. 1(a)[a] (the value is not marked in the paper)		Gap obtained from resistivity in Fig. 1(a)[a] (the value is not marked in the paper)		Gap obtained from STM at 300 K (∼630 meV) in Fig. 3(c)[b] or resistivity in (∼570 meV) in Fig. 12[k]	
	Gap obtained from calculations (∼858 meV, LSDA) in Fig. 2(a)[i] or (1370 meV, GGA) in Fig. 2[j]		–		Gap obtained from calculations of $Li_{1.1}(Zn_{0.875}Mn_{0.125})As$ (1516 meV, LSDA) in Fig. 4(c)[i]		Gap obtained from calculations (∼800 meV, LDA) in Figs. 5(a) and 5(b)[e] or (∼550 meV, GGA) in Fig. 17(a)[k]	

[a]Reference [2]; [b]Reference [153]; [c]Reference [195]; [d]Reference [201]; [e]Reference [202]; [f]Reference [203]; [g]Reference [204]; [h]Reference [205]; [i]Reference [206]; [j]Reference [207]; [k]Reference [208].

TABLE IV. Summarized results for DFSs $Li_{1+x}(Zn_{1-y}Mn_y)P$ systems. Note that the symbols for props, FIG, ct, semi-cond., and mag. are abbreviations for properties, figure, current work, semiconductor, and magnetization, respectively.

	LiZnP		$Li_{1.04}ZnP$		$Li_{1.04}(Zn_{0.9}Mn_{0.1})P$		LiMnP	
Compound	props	FIG.[Ref]	props	FIG.[Ref]	props	FIG.[Ref]	props	FIG. or Tab.[Ref]
Crystal	Cubic	1(a)[a]	Cubic	1(a)[a]	Cubic	1(a)[a]	Cubic	11(b)[cr]
Conductivity	Semi-Cond	5[b]	–	–	Semi-Cond	3(a)[a]	Semi-Cond	–
Mag. state	Non-mag.	–	Non-mag.	–	FM from dc mag.	2(a)[a]	AFM	Table I [cr]
Trans. temp	0	0	0	0	34 K	2(a)[a]	T_N=450.6 K	Table I [cr]
CMR	–	–	–	–	−32% (7 T, 13 K)	3(c)[a]	–	–
Band gap	Gap obtained from photoconductivity at 300 K (∼2100 meV) in Fig. 2(a)[c] or (∼2040 meV) in Fig. 4[b]		–		Gap obtained from resistivity in 1(a)[a] (the value is not marked in the paper)		–	
	Gap obtained from calculations (∼1350 meV, GGA) or (1940 meV, mBJ) in Table I [d]		–		–		Gap obtained from calculations (∼1290 meV, GGA)	

[a]Reference [40]; [b]Reference [209]; [c]Reference [201]; [d]Reference [210].

(a) Semiconducting behavior in $Na_{1.1}Mn_{0.25}$ system below SG $T_f = 12$ K (Fig. 1)

(b) Semiconducting behavior in AFM $Na_{1.12}Mn_{0.64}$ system above/below $T_N = 11$K (Fig. 1)

(c) Very large CMR in SG $Na_{1.1}Mn_{0.25}$, AFM $Na_{0.12}Mn_{0.64}$ systems at $T = 2$ K (Fig. 4)

(d) Energy gap for AFM and no gap for FM configurations in band calculations (Fig. 5)

Static SG or AFM spin configurations lead to semiconducting behaviors. Even dynamic spin fluctuations of AFM configurations promote semiconducting behavior, as indicated by the resistivity of AFM Na1.12 Mn0.64 system above T_N in Fig. 1. This is understandable since charge transport timescale is shorter than spin fluctuation timescale, and thus "dynamic" spin configurations could look like "static" to charge conduction phenomena. Metallic charge conduction can be obtained either by absence of magnetic impurities (in NaZnSb) or by ferromagnetic spin configuration in a high external magnetic field. Excess sodium (Na) in $Na_{1.1}ZnSb$ enhances metallic characteristics, while partial substitution of zinc (Zn) with manganese (Mn) in $Na_{1.1}(Zn_{0.75}Mn_{0.25})Sb$ results in semiconducting behavior. Conversion of metallic NaZnSb to semiconducting transport with (Zn,Mn) substitutions can be viewed as localization of metallic charges caused by the spin doping. However, the field-dependent CMR effect indicates that the nonmetallic behavior requires not only the

TABLE V. Summarized results for DFSs $(Ga_{1-x}Mn_x)As$ system. Note that the symbols for props, FIG, ct, semi-cond., and mag. are abbreviations for properties, figure, current work, semiconductor, and magnetization, respectively. It is noteworthy that pioneering research has successfully achieved CMR in (Ga,Mn)As systems through the application of defect engineering techniques, specifically ion irradiation [137,150,151].

	GaAs		$(Ga_{0.9995}Mn_{0.0005})As$		$(Ga_{0.985}Mn_{0.015})As$		$(Ga_{0.91}Mn_{0.09})As$		MnAs	
Compound	props	FIG.[Ref]	props	FIG.[Ref]	props	FIG.[Ref]	props	FIG.[Ref]	props	FIG.[Ref]
Crystal	Cubic	1(a)[a]	Cubic	S1[b]	Cubic	S1[b]	Cubic	S1[b]	Layer hexagonal	6[c]
Conductivity	Semi-Cond	43[a]	Semi-Cond	3(a)[b]	Metal	3(a)[b]	Metal	3(a)[b]	Metal	3[d]
Mag. state	Non-mag.	–	Non-mag.	3(f)[b]	FM	3(f)[b]	FM	3(f)[b]	FM	1[c]
Trans. temp	–	–	–	–	∼21 K	3(f)[b]	∼180 K	3(f)[b]	318 K (warming)	1[c]
CMR	–	–	–	–	∼4% (1 T, 4.2 K); ∼22.5% (18 T, 4.2 K);	S4(a)[b]	–	–	–	–
Band gap	Gap obtained from optical measurement (∼1423 meV, 300 K) in 43[a]		Gap obtained from electrical transport in Fig. 3(a)[b] (the value is not marked in the paper)		No gap obtained from electrical transport in Fig. 3(a)[b]		No gap obtained from electrical transport in Fig. 3(a)[b]		No gap obtained from electrical transport in Fig. 3[d]	
	Gap obtained from calculations (∼1429 meV, LDA)[f]		–		–		–		–	

[a]Reference [211]; [b]Reference [199]; [c]Reference [212]; [d]Reference [213]; [e]Reference [214].

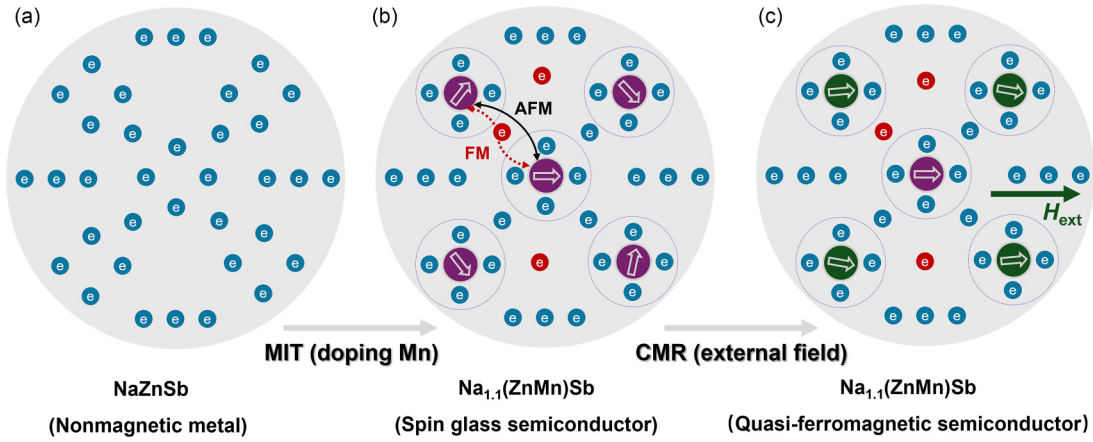

FIG. 12. Illustration of the charge responses MIT and CMR in response to spin doping and spin configuration in Na(Zn,Mn)Sb. The MIT transition occurs with the carrier localization from the parent nonmagnetic metal NaZnSb (a) to SG semiconductor $Na_{1.1}$(Zn, Mn)Sb (b). (c) The CMR phenomenon can be attributed to spin structure reorganization in response to strong external magnetic fields. The final magnetic state is determined by the competition between the ferromagnetic coupling of Mn-carrier-Mn (represented by red dash line) and the antiferromagnetic coupling of Mn-Mn (represented by black solid line). It is important to note that the "red" electron represents the excess charge carrier introduced by the additional sodium (Na). This contrasts with the primary charge carrier within the NaZnSb parent compound, which is indicated by the "green" electron.

existence of substituted Mn atoms but also the SG or AFM spin correlations and configurations of doped Mn moments.

This behavior can be called semiconductor or insulator to metal transition caused by the change of spin configurations, i.e., spin-driven MIT. In many Mott transition systems, such as $RENiO_3$ [187], the MIT is driven by structural phase transition, in "structure-driven MIT" and the spin configuration is determined in a more "passive" manner. Comparisons with (Ga,Mn)As, Li(Zn,Mn)As, and Li(Zn,Mn)P in Tables III–V, illustrate clear differences from Na(Zn,Mn)Sb found when magnetic order occurs into FM phase. In these systems, FM spin correlations "cooperate" with metallic behavior in MIT. In (Ga,Mn)As, the semiconductor to metal transition and the paramagnetic to ferromagnetic transition occur simultaneously in a cooperative fashion at Mn $\sim 4\%$ doping, In FM (Ga,Mn)As, Li(Zn,Mn)As and Li(Zn,Mn)P, we see only modest CMR effects caused by the external field.

B. Conclusion 2: A sharp second-order-like SG transition in Na(Zn,Mn)Sb

MuSR experiments demonstrated a rather sharp phase transition into the SG frozen state in Na(Zn,Mn)Sb as a function of temperature. This makes a clear contrast to ferromagnetic transitions in Li(Zn,Mn,Cu)As and Li(Zn,Mn)P which occur without dynamic critical behavior and are often associated with phase separation between volumes with ordered magnetic moments and dynamic spin fluctuations. The gradual change of FM volume fraction in Li-111 systems is reminiscent of the behavior seen in the intermediate AFM metal phase of "two step Mott transition" in $Ni(S, Se)_2$ [215] and $BaCoS_2/Ba(Co, Ni)S_2$ [193]. In these two Mott systems, the metallic conduction is already established while magnetic volume or the population of the ordered moment is determined in a percolation process. In Li-111 DMS and "two-step" Mott systems, the charge and spin transitions are decoupled. This may be a common origin of the absence of dynamic critical behavior, although the Li-111 DMS systems undergo FM order and the "two-step Mott" systems go to AFM order. It is very interesting to note that the SG transition into a highly disordered spin configurations occurs in a very sharp transition, while the transitions to a more uniform FM and AFM spin configurations, if occurring in materials containing strong disorder, exhibit broad first-order-like and possibly percolative transitions often associated with phase separation.

C. Conclusion 3: Additive effects of n.n. direct AFM coupling and metallic RKKY interaction

The first-principles calculation of the exchange interactions in Sec. D show that, with increasing charge and spin doping, the AFM direct exchange between the n.n. Mn pairs and the RKKY-like FM coupling due to doped charges effectively add up to determine the doping dependence of exchange interaction. The SG state of Na(Zn,Mn)As can be explained by a relatively strong AFM J_1 coupling surviving even after a significant charge doping reduces AFM J_1 and turns J_2, J_3, and $J_\perp$ to be ferromagnetic. One might tend to assume little change of the n.n. J_1 by the charge doping, while present results in Sec. D clearly indicate a strong effect of doped charges on all the exchange couplings. Figure 12 illustrates the metal to semiconductor evolution and subsequent recovery of metallic conduction via CMR by the application of external fields.

D. Correlations between coercive fields and geometrical AFM spin frustration

For (Ga,Mn)As and the "111" DMS systems, Tables II–V enabled detailed comparisons and characterization. In Table VI we extend such comparisons to include other DMS systems having tetragonal "122", hexagonal "122", and tetragonal "1111" structures. Among various properties, here

TABLE VI. Summarized results for (Ga,Mn)As system and new generation of DMSs with independent spin and charge doping mechanism. Note that the symbols H_C, M and ct, are abbreviations for coercive field, Bohr magneton per magnetic atom, and current work, respectively.

Family	Structure	compound	T_C or T_f (K)	Coercive field H_C (G)	M (μ_B/Mn or μ_B/Co)	CMR	$T \to 0$ K, $4/3\alpha_s$ (μs^{-1})	Transition type	MIT
'11'	$F\bar{4}3m$	$(Ga_{0.964}Mn_{0.034})As$[a]	$T_C = 46$	–	–	–	~28.2 (ag)	First order	Yes
		$(Ga_{0.953}Mn_{0.047})As$[b]	$T_C = 58$	~150 at 5 K	–	~7.0% at 5 K, 5 T	–		
		$(Ga_{0.93}Mn_{0.07})As$[a]	$T_C = 96$	–	–	–	~40.1(ag)		
'111'	$P4/mmm$	$Na_{1.1}(Zn_{0.75}Mn_{0.05})Sb$ [cr]	$T_f = 12$	~8400 at 2 K	~0.44 at 2 K	~99.9% at 2 K, 7 T	~8.3	Second order	Yes
	$F\bar{4}3m$	$Li_{1.1}(Zn_{0.95}Mn_{0.05})As$ [cr],c	$T_C = 29$	~30 at 2 K	~2.10 at 2 K		~15.7	First order	Yes
		$Li_{1.05}(Zn_{0.9}Mn_{0.1})As$ [cr],c	$T_C = 22$	–	~0.60 at 2 K		~11.0		
	$F\bar{4}3m$	$Li_{1.04}(Zn_{0.9}Mn_{0.1})P$ [cr],d	$T_C = 34$	~50 at 2 K	~0.60 at 2 K	~32.0% at 13 K, 7 T	~2.1	First order	Yes
		$Li_{1.15}(Zn_{0.9}Mn_{0.1})P$ [cr],e	$T_C = 22$	~20 at 5 K	~0.22 at 5 K	–	~3.1		
	$F\bar{4}3m$	$Li(Zn_{0.7}Mn_{0.15}Cu_{0.15})As$ [cr],f	$T_C = 23$	–	–	–	~5.9	First order	Yes
		$Li(Zn_{0.75}Mn_{0.125}Cu_{0.125})As$ [cr],f	$T_C = 33$	~40 at 5 K	~0.53 at 2 K		~13.7		
'122'	I4/mmm	$(Ba_{0.8}K_{0.2})(Zn_{0.9}Mn_{0.1})_2As_2$[g]	$T_C = 135$	~17000 at 2 K	~1.10 at 2 K	–	~47.0	First order	Yes
		$(Ba_{0.7}K_{0.3})(Zn_{0.85}Mn_{0.15})_2As_2$[h]	$T_C = 230$	~13000 at 2 K	~1.03 at 2 K	~7.5% at 13 K, 7 T	–		
	I4/mmm	$Ba(Zn_{0.95}Co_{0.05})_2As_2$[i]	$T_C = 41$	~11 at 2 K	~0.22 at 2 K	–	~0.5	–	–
	$P\bar{3}m1$	$(Ca_{0.9}Na_{0.1})(Zn_{0.95}Mn_{0.05})_2As_2$[g]	$T_C = 40$	~105 at 2 K	~1.90 at 2 K	~7.8% at 2 K, 7 T	~33	First order	Yes
	$P\bar{3}m1$	$(Sr_{0.8}Na_{0.2})(Zn_{0.85}Mn_{0.15})_2As_2$[k]	$T_C = 24$	~100 at 2 K	~0.60 at 2 K	–	~42	First order	Yes
'1111'	P4/nmm		$T_C = 35$	~10600 at 2 K	~1.85 at 2 K	–	~9.3	–	Yes
		$(La_{0.95}Ba_{0.05})(Zn_{0.95}Mn_{0.05})AsO$[l]							
		$(La_{0.90}Ba_{0.1})(Zn_{0.9}Mn_{0.1})AsO$[l]	$T_C = 40$	~11400 at 2 K	~1.50 at 2 K		~16.0		
	P4/nmm	$(La_{0.90}Ca_{0.1})(Zn_{0.9}Mn_{0.1})As$[m]	$T_C = 30$	~9700 at 5 K	~1.40 at 5 K	–	~15.6	–	Yes
	P4/nmm	$(Ba_{0.85}K_{0.15})F(Zn_{0.9}Mn_{0.1})As$[n]	$T_C = 20$	–	–	–	~11.4	First order	Yes
		$(Ba_{0.8}K_{0.20})F(Zn_{0.95}Mn_{0.05})As$[n]	$T_C = 12$	~8000 at 5 K	~0.80 at 5 K	~29.0% at 30 K, 7 T	–		

[a]Reference [36]; [b]Reference [216]; [c]Reference [2]; [d]Reference [40]; [e]Reference [3]; [f]Reference [4]; [g]Reference [47]; [h]Reference [53]; [i]Reference [77]; [g]Reference [54]; [k]Reference [48]; [l]Reference [41]; [m]Reference [62]; [n]Reference [59].

we focus on coercive field values and propose a general argument. In Table VI we notice two different groups of Mn doped DMS systems. Very small coercive fields 50–200 G have been observed for (Ga,Mn)As, Li(Zn,Mn,Cu)As, Li(Zn,Mn)P, and hexagonal 122 systems $(Ca_{0.9}Na_{0.1})(Zn_{0.95}Mn_{0.05})_2As_2$ and $(Sr_{0.8}Na_{0.2})(Zn_{0.85}Mn_{0.15})_2As_2$. For the n.n. direct AFM exchange coupling, these systems have geometrical frustration, since Mn atoms are located in an FCC lattice in the cubic DMS systems including (Ga,Mn)As, and on a triangular configuration in two-dimensional planes in hexagonal 122 DMS systems. In contrast, very high coercive fields of several kG to several tesla have been observed in layered tetragonal Na(Zn,Mn)As, tetragonal 122, and tetragonal 1111 DMS systems. None of these tetragonal systems involve geometrical frustration of the n.n. AFM interaction. This classification works without any exception for all the DMS systems including Mn listed in Table VI, regardless of whether their spin structures are FM or SG. For many years, the origin of the widely different coercive field values in DMS systems has remained as an unresolved mystery. Here we found an empirical rule that a very small coercive field is related to a lattice structure in which the Mn AFM exchange couplings are geometrically frustrated.

It is rather surprising to see that the coercive field of relatively dilute Mn moments with 5%–20% coverage of Zn sites in FM and SG networks is related to spin frustration of n.n. AFM pairs. The statistical probability would be very low of finding at least three n.n. sites all occupied by Mn on the dilute Mn spin network of the listed DMS systems. Yet, it seems that the anisotropy energy arising from nonfrustrated AFM distinguish between the low and high coercive fields. This may be hinting that even on the FM or SG network of Mn moments, there could be a small number of spin clusters with nearly AFM local spin configurations, perhaps in the dangling end locations. For geometrically frustrated AFM lattices, the energy cost to alter the spin orientations of such clusters can be significantly lower than on the lattices without geometrical frustration. The local spin configurations and resulting anisotropy energy in relatively dilute DMS spin networks could be an interesting research subject for computer simulations in the future. Local spin configurations could be very different from FM configurations even in a spin network having significant average FM magnetization.

VII. CONCLUSIONS

In this study we conduct a systematic investigation of spin-charge interactions in SG compound Na(Zn,Mn)Sb and related FM DMSs through a series of multiprobe measurements, which include magnetometry, magnetotransport,

ARPES, STM, and μSR. Our findings are further substantiated by first-principles calculations. This paper presents detailed comparisons and analyses across various families and generations of DMS systems, providing evidence for spin-driven MIT, CMR, dynamic critical behavior, and second-order phase transitions in Na(Zn,Mn)As. Furthermore, it offers a comprehensive understanding of the similarities and differences among the three generations of DMS systems. These results illuminate new perspectives and may serve as a canonical reference within the DMS research community.

ACKNOWLEDGMENTS

This project was financially supported by National Key Research and Development Projects of China (Grants No. 2022YFA1405100 and No. 2022YFA1204100), the National Natural Science Foundation of China (Grants No. 12074378 and No. 61888102), and Chinese Academy of Sciences (Grants No. YSBR-030, No. JZHKYPT-2021-08, and No. XDB33000000). The work at Columbia was supported by DMR 2104661 by the US National Science Foundation. G.Q.Z. has received partial support from the China Scholarship Council (No. 201904910900), the Plan of Assistant to Special Researcher at the University of Chinese Academy of Sciences (2022-PASR-202206), and the Chinese Academy of Sciences Project for Young Scientists in Basic Research (2022YSBR-048). We thank T. Goko, H. Luetkens, and E. Morenzoni's technical support for the ZF- and wTF- μSR measurement of $Li_{1.15}(Zn_{0.9}Mn_{0.1})P$ in PSI at 2013. We acknowledge discussions by Prof. Fuchun Zhang, Prof. Igro Zuric, Prof. Yongxin Pan, Prof. Yongqing Li, Prof. Sheng Meng, Prof. Kui Jin, and Prof. Graeme Luke.

The project was conceived by G.Q.Z., in consultation with Y.J.U. and B.G. G.Q.Z., S.Y., Z.D., S.L.G., F.L.N., and C.Q.J. synthesized all these materials. Transport measurements were performed by G.Q.Z., S.Y., and C.Q.J. ARPES by Y.H. and X.J.Z. STM measurements by H.C., Y.Q.X. and H.-J.G. The μSR data were collected by G.Q.Z., Y.P.C., K.M.K., S.L.G., F.L.N., and Y.J.U., and analyzed by G.Q.Z. and Y.J.U. The calculation for exchange interaction plan was proposed by G.Q.Z. and performed by X.L. in consultation with B.G. and G.S. S.M. contributed in analyses of transport results and theoretical calculations. G.Q.Z. and Y.J.U. generated a draft of the manuscript with initial inputs from X.L., H.C., and Y.H., which was then circulated to all the authors for their revisions and approval. All authors reviewed the manuscript and approved.

The authors declare no competing interests.

[1] S. Yu, Y. Peng, G. Zhao, J. Zhao, X. Wang, J. Zhang, Z. Deng, and C. Jin, Colossal negative magnetoresistance in spin glass Na(Zn,Mn)Sb, J. Semicond. **44**, 032501 (2023).

[2] Z. Deng, C. Q. Jin, Q. Q. Liu, X. C. Wang, J. L. Zhu, S. M. Feng, L. C. Chen, R. C. Yu, C. Arguello, T. Goko *et al.*, Li(Zn,Mn)as as a new generation ferromagnet based on a I-II-V semiconductor, Nat. Commun. **2**, 422 (2011).

[3] F. L. Ning, H. Man, X. Gong, G. Zhi, S. Guo, C. Ding, Q. Wang, T. Goko, L. Liu, B. A. Frandsen *et al.*, Suppression of T_c by overdoped li in the diluted ferromagnetic semiconductor $Li_{1+y}(Zn_{1-x}Mn_x)P$: A μSR investigation, Phys. Rev. B **90**, 085123 (2014).

[4] S. L. Guo, Y. Zhao, H. Y. Man, C. Ding, X. Gong, G. X. Zhi, L. C. Fu, Y. L. Gu, B. A. Frandsen, L. Liu *et al.*, μSR investigation of a new diluted magnetic semiconductor Li(Zn,Mn,Cu)As with Mn and Cu codoping at the same Zn sites, J. Phys.: Condens. Matter **28**, 366001 (2016).

[5] T. Kasuya and A. Yanase, Anomalous transport phenomena in Eu-chalcogenide alloys, Rev. Mod. Phys. **40**, 684 (1968).

[6] J. K. Furdyna, Diluted magnetic semiconductors, J. Appl. Phys. **64**, R29 (1988).

[7] T. Dietl and H. Ohno, Dilute ferromagnetic semiconductors: Physics and spintronic structures, Rev. Mod. Phys. **86**, 187 (2014).

[8] X. Li, S. Qi, F. Jiang, Z. Quan, and X. Xu, Diluted magnetic oxides, Sci. China: Phys., Mech. Astron. **56**, 111 (2012).

[9] I. Žutić, J. Fabian, and S. D. Sarma, Spintronics: fundamentals and applications, Rev. Mod. Phys. **76**, 323 (2004).

[10] D. D. Awschalom and M. E. Flatte, Challenges for semiconductor spintronics, Nat. Phys. **3**, 153 (2007).

[11] T. Dietl, A. Bonanni, and H. Ohno, Families of magnetic semiconductors—An overview, J. Semicond. **40**, 080301 (2019).

[12] E. Y. Tsymbal and I. In Žutić, *Handbook of Spin Transport and Magnetism* (Chapman and Hall/CRC, New York, 2011).

[13] J. A. Gaj and J. Kossut, *Introduction to the Physics of Diluted Magnetic Semiconductors* (Springer, Berlin, 2010).

[14] D. D. Awschalom, D. Loss, and P. N. Samarth, *Semiconductor Spintronics and Quantum Computation* (Spinger, Berlin, 2002).

[15] D. D. A. Yongbing Xu and Junsaku Nitta, *Handbook of Spintronics* (Spinger, Berlin, 2016).

[16] M. Król, R. Mirek, K. Lekenta, J.-G. Rousset, D. Stephan, M. Nawrocki, M. Matuszewski, J. Szczytko, W. Pacuski, and B. Piętka, Spin polarized semimagnetic exciton-polariton condensate in magnetic field, Sci. Rep. **8**, 6694 (2018).

[17] C. Betthausen, P. Giudici, A. Iankilevitch, C. Preis, V. Kolkovsky, M. Wiater, G. Karczewski, B. A. Piot, J. Kunc, M. Potemski *et al.*, Fractional quantum Hall effect in a dilute magnetic semiconductor, Phys. Rev. B **90**, 115302 (2014).

[18] T. Dietl, Hole states in wide band-gap diluted magnetic semiconductors and oxides, Phys. Rev. B **77**, 085208 (2008).

[19] R. Fiederling, M. Keim, G. Reuscher, W. Ossau, G. Schmidt, A. Waag, and L. W. Molenkamp, Injection and detection of a spin-polarized current in a light-emitting diode, Nature (London) **402**, 787 (1999).

[20] Y. Ohno, D. K. Young, B. Beschoten, F. Matsukura, H. Ohno, and D. D. Awschalom, Electrical spin injection in a ferromagnetic semiconductor heterostructure, Nature (London) **402**, 790 (1999).

[21] T. Taniyama, E. Wada, M. Itoh, and M. Yamaguchi, Electrical and optical spin injection in ferromagnet/semiconductor heterostructures, NPG Asia Mater. **3**, 65 (2011).

[22] B. Leclercq, C. Rigaux, A. Mycielski, and M. Menant, Critical dynamics in $Cd_{1-x}Mn_xTe$ spin glasses, Phys. Rev. B **47**, 6169 (1993).

[23] J. Jaroszynski, J. Wrobel, G. Karczewski, T. Wojtowicz, and T. Dietl, Magnetoconductance noise and irreversibilities in submicron wires of spin-glass n^+-$Cd_{1-x}Mn_xTe$, Phys. Rev. Lett. **80**, 5635 (1998).

[24] W. Pacuski, P. Kossacki, D. Ferrand, A. Golnik, J. Cibert, M. Wegscheider, A. Navarro-Quezada, A. Bonanni, M. Kiecana, M. Sawicki *et al.*, Observation of strong-coupling effects in a diluted magnetic semiconductor $Ga_{1-x}Fe_xN$, Phys. Rev. Lett. **100**, 037204 (2008).

[25] T. Jungwirth, J. Sinova, J. Mašek, J. Kučera, and A. H. MacDonald, Theory of ferromagnetic (III,Mn)V semiconductors, Rev. Mod. Phys. **78**, 809 (2006).

[26] T. Jungwirth, J. Wunderlich, V. Novák, K. Olejník, K. Olejník, B. L. Gallagher, R. P. Campion, and K. W. Edmonds, Spin-dependent phenomena and device concepts explored in (Ga,Mn)As, Rev. Mod. Phys. **86**, 855 (2014).

[27] T. Dietl, K. Sato, T. Fukushima, A. Bonanni, M. Jamet, A. Barski, S. Kuroda, M. Tanaka, P. N. Hai, and H. Katayama-Yoshida, Spinodal nanodecomposition in semiconductors doped with transition metals, Rev. Mod. Phys. **87**, 1311 (2015).

[28] T. Dietl, A ten-year perspective on dilute magnetic semiconductors and oxides, Nat. Mater. **9**, 965 (2010).

[29] H. Ohno, A. Shen, F. Matsukura, A. Oiwa, A. Endo, S. Katsumoto, and Y. Iye, (Ga,Mn)As: A new diluted magnetic semiconductor based on GaAs, Appl. Phys. Lett. **69**, 363 (1996).

[30] L. Chen, X. Yang, F. Yang, J. Zhao, J. Misuraca, P. Xiong, and S. von Molnar, Enhancing the Curie temperature of ferromagnetic semiconductor (Ga,Mn)As to 200 K via nanostructure engineering, Nano Lett. **11**, 2584 (2011).

[31] T. Dietl, H. Ohno, F. Matsukura, J. Cibert, and D. Ferrand, Zener model description of ferromagnetism in zinc-blende magnetic semiconductors, Science **287**, 1019 (2000).

[32] T. Dietl, J. Cibert, P. Kossacki, D. Ferrand, S. Tatarenko, A. Wasiela, Y. M. d'aubigne, F. Matsukura, N. Akiba, and H. Ohno, Ferromagnetism induced by free carriers in *p*-type structures of diluted magnetic semiconductors, Phys. E (Amsterdam, Neth.) **7**, 967 (2000).

[33] K. S. Burch, D. D. Awschalom, and D. N. Basov, Optical properties of III-Mn-V ferromagnetic semiconductors, J. Magn. Magn. Mater. **320**, 3207 (2008).

[34] N. Samarth, Ferromagnetic semicondutors: Battle of the bands, Nat. Mater. **11**, 360 (2012).

[35] J. Fujii, B. R. Salles, M. Sperl, S. Ueda, M. Kobata, K. Kobayashi, Y. Yamashita, P. Torelli, M. Utz, C. S. Fadley *et al.*, Identifying the electronic character and role of the Mn states in the valence band of (Ga,Mn)As, Phys. Rev. Lett. **111**, 097201 (2013).

[36] S. R. Dunsiger, J. P. Carlo, T. Goko, G. Nieuwenhuys, T. Prokscha, A. Suter, E. Morenzoni, D. Chiba, Y. Nishitani, T. Tanikawa *et al.*, Spatially homogeneous ferromagnetism of (Ga,Mn)As, Nat. Mater. **9**, 299 (2010).

[37] V. G. Storchak, D. G. Eshchenko, E. Morenzoni, T. Prokscha, A. Suter, X. Liu, and J. K. Furdyna, Spatially resolved inhomogeneous ferromagnetism in (Ga,Mn)As diluted magnetic semiconductors: A microscopic study by muon spin relaxation, Phys. Rev. Lett. **101**, 027202 (2008).

[38] B. J. Kirby, J. A. Borchers, J. J. Rhyne, S. G. Te Velthuis, A. Hoffmann, K. V. O'Donovan, T. Wojtowicz, X. Liu, W. L. Lim, and J. K. Furdyna, Annealing-dependent magnetic depth profile in $(Ga_{1-x}Mn_x)As$, Phys. Rev. B **69**, 081307(R) (2004).

[39] J. Masek, J. Kudrnovsky, F. Maca, B. L. Gallagher, R. P. Campion, D. H. Gregory, and T. Jungwirth, Dilute moment *n*-type ferromagnetic semiconductor Li(Zn,Mn)As, Phys. Rev. Lett. **98**, 067202 (2007).

[40] Z. Deng, K. Zhao, B. Gu, W. Han, J. L. Zhu, X. C. Wang, X. Li, Q. Q. Liu, R. C. Yu, T. Goko *et al.*, Diluted ferromagnetic semiconductor Li(Zn,Mn)P with decoupled charge and spin doping, Phys. Rev. B **88**, 081203(R) (2013).

[41] C. Ding, H. Man, C. Qin, J. Lu, Y. Sun, Q. Wang, B. Yu, C. Feng, T. Goko, C. J. Arguello *et al.*, $(La_{1-x}Ba_x)(Zn_{1-x}Mn_x)AsO$: A two-dimensional 1111-type diluted magnetic semiconductor in bulk form, Phys. Rev. B **88**, 041102(R) (2013).

[42] C. Ding, C. Qin, H. Y. Man, T. Imai, and F. L. Ning, NMR investigation of the diluted magnetic semiconductor $Li(Zn_{1-x}Mn_x)P$ ($x = 0.1$), Phys. Rev. B **88**, 041108(R) (2013).

[43] W. Han, K. Zhao, X. Wang, Q. Liu, F. Ning, Z. Deng, Y. Liu, J. Zhu, C. Ding, H. Man *et al.*, Diluted ferromagnetic semiconductor (LaCa)(ZnMn)SbO isostructural to "1111" type iron pnictide superconductors, Sci. China: Phys. Mech. Astron. **56**, 2026 (2013).

[44] J. Lu, H. Man, C. Ding, Q. Wang, B. Yu, S. Guo, H. Wang, B. Chen, W. Han, C. Jin *et al.*, The synthesis and characterization of 1111-type diluted magnetic semiconductors $(La_{1-x}Sr_x)(Zn_{1-x}TM_x)AsO$ (TM = Mn, Fe, Co), Europhys. Lett. **103**, 67011 (2013).

[45] X. Yang, Y. Li, C. Shen, B. Si, Y. Sun, Q. Tao, G. Cao, Z. Xu, and F. Zhang, Sr and Mn co-doped LaCuSo: A wide band gap oxide diluted magnetic semiconductor with T_c around 200 K, Appl. Phys. Lett. **103**, 022410 (2013).

[46] X. Yang, Y. Li, P. Zhang, H. Jiang, Y. Luo, Q. Chen, C. Feng, C. Cao, J. Dai, Q. Tao *et al.*, K and Mn co-doped $BaCd_2As_2$: A hexagonal structured bulk diluted magnetic semiconductor with large magnetoresistance, J. Appl. Phys. **114**, 223905 (2013).

[47] K. Zhao, Z. Deng, X. C. Wang, W. Han, J. L. Zhu, X. Li, Q. Q. Liu, R. C. Yu, T. Goko, B. Frandsen *et al.*, New diluted ferromagnetic semiconductor with curie temperature up to 180 K and isostructural to the '122' iron-based superconductors, Nat. Commun. **4**, 1442 (2013).

[48] B. J. Chen, K. Zhao, Z. Deng, W. Han, J. L. Zhu, X. C. Wang, Q. Q. Liu, B. Frandsen, L. Liu, S. Cheung *et al.*, $(Sr, Na)(Zn, Mn)_2As_2$: A diluted ferromagnetic semiconductor with the hexagonal $CaAl_2Si_2$ type structure, Phys. Rev. B **90**, 155202 (2014).

[49] C. Ding, X. Gong, H. Man, G. Zhi, S. Guo, Y. Zhao, H. Wang, B. Chen, and F. L. Ning, The suppression of Curie temperature by Sr doping in diluted ferromagnetic semiconductor $(La_{1-x}Sr_x)(Zn_{1-y}Mn_y)AsO$, Europhys. Lett. **107**, 17004 (2014).

[50] H. Man, C. Qin, C. Ding, Q. Wang, X. Gong, S. Guo, H. Wang, B. Chen, and F. L. Ning, $(Sr_3La_2O_5)(Zn_{1-x}Mn_x)_2As_2$: A bulk form diluted magnetic semiconductor isostructural to the "32522" Fe-based superconductors, Europhys. Lett. **105**, 67004 (2014).

[51] Q. Wang, H. Y. Man, C. Ding, X. Gong, S. L. Guo, H. K. Jin, H. D. Wang, B. Chen, and F. L. Ning, $Li_{1.1}(Zn_{1-x}Cr_x)As$: Cr

doped I-II-V diluted magnetic semiconductors in bulk form, J. Appl. Phys. **115**, 083917 (2014).

[52] X. Yang, Q. Chen, Y. Li, Z. Wang, J. Bao, Y. Li, Q. Tao, G. Cao, and Z.-A. Xu, $Sr_{0.9}K_{0.1}Zn_{1.8}Mn_{0.2}As_2$: A ferromagnetic semiconductor with colossal magnetoresistance, Europhys. Lett. **107**, 67007 (2014).

[53] K. Zhao, B. Chen, G. Zhao, Z. Yuan, Q. Liu, Z. Deng, J. Zhu, and C. Jin, Ferromagnetism at 230 K in $(Ba_{0.7}K_{0.3})(Zn_{0.85}Mn_{0.15})_2As_2$ diluted magnetic semiconductor, Chin. Sci. Bull. **59**, 2524 (2014).

[54] K. Zhao, B. J. Chen, Z. Deng, W. Han, G. Q. Zhao, J. L. Zhu, Q. Q. Liu, X. C. Wang, B. Frandsen, L. Liu *et al.*, (Ca, Na)(Zn, Mn)$_2As_2$: A new spin and charge doping decoupled diluted ferromagnetic semiconductor, J. Appl. Phys. **116**, 163906 (2014).

[55] H. Man, S. Guo, Y. Sui, Y. Guo, B. Chen, H. Wang, C. Ding, and F. L. Ning, $Ba(Zn_{1-2x}Mn_xCu_x)_2As_2$: A bulk form diluted ferromagnetic semiconductor with Mn and Cu codoping at Zn sites, Sci. Rep. **5**, 15507 (2015).

[56] H. Suzuki, G. Q. Zhao, K. Zhao, B. J. Chen, M. Horio, K. Koshiishi, J. Xu, M. Kobayashi, M. Minohara, E. Sakai *et al.*, Fermi surfaces and *p-d* hybridization in the diluted magnetic semiconductor $Ba_{1-x}K_x(Zn_{1-y}Mn_y)_2As_2$ studied by soft x-ray angle-resolved photoemission spectroscopy, Phys. Rev. B **92**, 235120 (2015).

[57] H. Suzuki, K. Zhao, G. Shibata, Y. Takahashi, S. Sakamoto, K. Yoshimatsu, B. J. Chen, H. Kumigashira, F. H. Chang, H. J. Lin *et al.*, Photoemission and x-ray absorption studies of the isostructural to Fe-based superconductors diluted magnetic semiconductor $(Ba_{1-x}K_x)(Zn_{1-y}Mn_y)_2As_2$, Phys. Rev. B **91**, 140401 (2015).

[58] B. Chen, Z. Deng, W. Li, M. Gao, Z. Li, G. Zhao, S. Yu, X. Wang, Q. Liu, and C. Jin, $(Sr_{1-x}Na_x)(Cd_{1-x}Mn_x)_2As_2$: A new charge and spin doping decoupled diluted magnetic semiconductors with $CaAl_2Si_2$-type structure, J. Appl. Phys. **120**, 083902 (2016).

[59] B. Chen, Z. Deng, W. Li, M. Gao, Q. Liu, C. Z. Gu, F. X. Hu, B. G. Shen, B. Frandsen, S. Cheung *et al.*, New fluoride-arsenide diluted magnetic semiconductor (Ba,K)F(Zn,Mn)As with independent spin and charge doping, Sci. Rep. **6**, 36578 (2016).

[60] B. Chen, Z. Deng, W. Li, M. Gao, J. Zhao, G. Zhao, S. Yu, X. Wang, Q. Liu, and C. Jin, Li(Zn,Co,Mn)As: A bulk form diluted magnetic semiconductor with co and Mn co-doping at Zn sites, AIP Adv. **6**, 115014 (2016).

[61] B.-J. Chen, Z. Deng, X.-C. Wang, S.-M. Feng, Z. Yuan, S.-J. Zhang, Q.-Q. Liu, and C.-Q Jin, Structural stability at high pressure, electronic, and magnetic properties of bafznas: A new candidate of host material of diluted magnetic semiconductors, Chin. Phys. B **25**, 077503 (2016).

[62] C. Ding, S. Guo, Y. Zhao, H. Man, L. Fu, Y. Gu, Z. Wang, L. Liu, B. A. Frandsen, S. Cheung *et al.*, The synthesis and characterization of 1111 type diluted ferromagnetic semiconductor $(La_{1-x}Ca_x)(Zn_{1-x}Mn_x)AsO$, J. Phys.: Condens. Matter **28**, 026003 (2016).

[63] B. A. Frandsen, Z. Gong, M. W. Terban, S. Banerjee, B. Chen, C. Jin, M. Feygenson, Y. J. Uemura, and S. J. L. Billinge, Local atomic and magnetic structure of dilute magnetic semiconductor (Ba, K)(Zn, Mn)$_2As_2$, Phys. Rev. B **94**, 094102 (2016).

[64] S. Guo, H. Man, X. Gong, C. Ding, Y. Zhao, B. Chen, Y. Guo, H. Wang, and F. L. Ning, $(Ba_{1-x}K_x)(Cu_{2-x}Mn_x)Se_2$: A copper-based bulk form diluted magnetic semiconductor with orthorhombic $BaCu_2S_2$-type structure, J. Magn. Magn. Mater. **400**, 295 (2016).

[65] S. Guo, Y. Zhao, X. Gong, H. Man, C. Ding, G. Zhi, L. Fu, Y. Gu, H. Wang, B. Chen *et al.*, $La(Zn_{1-2x}Mn_xCu_x)AsO$: A 1111-type diluted magnetic semiconductor with manganese and copper codoping at Zn sites, EPL **114**, 57008 (2016).

[66] F. Sun, N. N. Li, B. J. Chen, Y. T. Jia, L. J. Zhang, W. M. Li, G. Q. Zhao, L. Y. Xing, G. Fabbris, Y. G. Wang *et al.*, Pressure effect on the magnetism of the diluted magnetic semiconductor $(Ba_{1-x}K_x)(Zn_{1-y}Mn_y)_2As_2$ with independent spin and charge doping, Phys. Rev. B **93**, 224403 (2016).

[67] F. Sun, C. Xu, S. Yu, B.-J. Chen, G.-Q. Zhao, Z. Deng, W.-G. Yang, and C.-Q. Jin, Synchrotron x-ray diffraction studies on the new generation ferromagnetic semiconductor Li(Zn,Mn)as under high pressure, Chin. Phys. Lett. **34**, 067501 (2017).

[68] F. Sun, G. Q. Zhao, C. A. Escanhoela, B. J. Chen, R. H. Kou, Y. G. Wang, Y. M. Xiao, P. Chow, H. K. Mao, D. Haskel *et al.*, Hole doping and pressure effects on the II-II-V-based diluted magnetic semiconductor $(Ba_{1-x}K_x)(Zn_{1-y}Mn_y)_2As_2$, Phys. Rev. B **95**, 094412 (2017).

[69] R. Wang, Z. X. Huang, G. Q. Zhao, S. Yu, Z. Deng, C. Q. Jin, Q. J. Jia, Y. Chen, T. Y. Yang, X. M. Jiang *et al.*, Out-of-plane easy-axis in thin films of diluted magnetic semiconductor $Ba_{1-x}K_x(Zn_{1-y}Mn_y)_2As_2$, AIP Adv. **7**, 045017 (2017).

[70] G. Q. Zhao, C. J. Lin, Z. Deng, G. X. Gu, S. Yu, X. C. Wang, Z. Z. Gong, Y. J. Uemura, Y. Q. Li, and C. Q. Jin, Single crystal growth and spin polarization measurements of diluted magnetic semiconductor (BaK)$(ZnMn)_2As_2$, Sci. Rep. **7**, 14473 (2017).

[71] Y. Zhao, K. Wang, S. Guo, L. Fu, Y. Gu, G. Zhi, L. Xu, Q. Cui, J. Cheng, H. Wang *et al.*, $La(Zn_{1-2x}Mn_xCu_x)SbO$: A new diluted magnetic semiconductor isostructural to 1111-type iron pnictide superconductors, Europhys. Lett. **120**, 47005 (2017).

[72] F. Zhu, W. X. Jiang, P. Li, Z. Q. Yang, H. Y. Man, Y. Y. Li, C. Liu, D. Guan, J.-F. Jia, F. L. Ning *et al.*, Electronic structure of $Ba(Zn_{0.875}Mn_{0.125})_2As_2$, Appl. Phys. Lett. **111**, 062106 (2017).

[73] G. Gu, G. Zhao, C. Lin, Y. Li, C. Jin, and G. Xiang, Asperomagnetic order in diluted magnetic semiconductor (Ba, Na)(Zn, Mn)$_2As_2$, Appl. Phys. Lett. **112**, 032402 (2018).

[74] M. A. Surmach, B. J. Chen, Z. Deng, C. Q. Jin, J. K. Glasbrenner, I. I. Mazin, A. Ivanov, and D. S. Inosov, Weak doping dependence of the antiferromagnetic coupling between nearest-neighbor Mn^{2+} spins in $(Ba_{1-x}K_x)(Zn_{1-y}Mn_y)_2As_2$, Phys. Rev. B **97**, 104418 (2018).

[75] G. Q. Zhao, Z. Li, F. Sun, Z. Yuan, B. J. Chen, S. Yu, Y. Peng, Z. Deng, X. C. Wang, and C. Q. Jin, Effects of high pressure on the ferromagnetism and in-plane electrical transport of $(Ba_{0.904}K_{0.096})(Zn_{0.805}Mn_{0.195})_2As_2$ single crystal, J. Phys.: Condens. Matter **30**, 254001 (2018).

[76] L. Fu, Y. Gu, S. Guo, K. Wang, H. Zhang, G. Zhi, H. Liu, Y. Xu, Y. Wang, H. Wang *et al.*, Ferromagnetism in fluoride-antimonide $SrF(Zn_{1-2x}Mn_xCu_x)Sb$ with a quasi two dimensional structure, J. Magn. Magn. Mater. **483**, 95 (2019).

[77] S. Guo, H. Man, K. Wang, C. Ding, Y. Zhao, L. Fu, Y. Gu, G. Zhi, B. A. Frandsen, S. C. Cheung *et al.*, Ba(Zn, Co)$_2As_2$: A diluted ferromagnetic semiconductor with *n*-type carriers and

isostructural to 122 iron-based superconductors, Phys. Rev. B **99**, 155201 (2019).

[78] W. Han, B. J. Chen, B. Gu, G. Q. Zhao, S. Yu, X. C. Wang, Q. Q. Liu, Z. Deng, W. M. Li, J. F. Zhao *et al.*, Li(Cd,Mn)P: A new cadmium based diluted ferromagnetic semiconductor with independent spin & charge doping, Sci. Rep. **9**, 7490 (2019).

[79] Y. Peng, S. Yu, G. Q. Zhao, W. M. Li, J. F. Zhao, L. P. Cao, X. C. Wang, Q. Q. Liu, S. J. Zhang, R. Z. Yu *et al.*, Effects of chemical pressure on diluted magnetic semiconductor (Ba, K)$(Zn, Mn)_2As_2$, Chin. Phys. B **28**, 057501 (2019).

[80] S. Yu, G. Zhao, Y. Peng, X. Zhu, X. Wang, J. Zhao, L. Cao, W. Li, Z. Li, Z. Deng *et al.*, A substantial increase of curie temperature in a new type of diluted magnetic semiconductors via effects of chemical pressure, APL Mater. **7**, 101119 (2019).

[81] Y. Gu, H. Zhang, R. Zhang, L. Fu, K. Wang, G. Zhi, S. Guo, and F. Ning, A novel diluted magnetic semiconductor (Ca, Na)$(Zn, Mn)_2Sb_2$ with decoupled charge and spin dopings, Chin. Phys. B **29**, 057507 (2020).

[82] X. Shen, Z. Deng, Z. Li, B. Gu, L. H. He, Y. Yao, C. Q. Jin, and R. C. Yu, Effects of structure modulation on the magnetic properties in diluted magnetic semiconductor $Li_{1+y}Zn_{0.9}Mn_{0.1}As_{1.0}$, Phys. Rev. Mater. **4**, 094412 (2020).

[83] S. Yu, X. Liu, G. Zhao, Y. Peng, X. Wang, J. Zhao, W. Li, Z. Deng, J. K. Furdyna, Y. J. Uemura *et al.*, Anomalous critical point behavior in dilute magnetic semiconductor (Ca, Na)$(Zn, Mn)_2Sb_2$, Phys. Rev. Mater. **4**, 024411 (2020).

[84] S. Yu, G. Zhao, Y. Peng, X. Wang, Q. Liu, R. Yu, S. Zhang, J. Zhao, W. Li, Z. Deng *et al.*, (Ba, K)$(Zn, Mn)_2Sb_2$: A new type of diluted magnetic semiconductor, Crystals **10**, 690 (2020).

[85] L. Fu, Y. Gu, G. Zhi, H. Zhang, R. Zhang, J. Dong, X. Zhao, L. Xie, and F. Ning, Drastic improvement of Curie temperature by chemical pressure in *n*-type diluted magnetic semiconductor Ba$(Zn, Co)_2As_2$, Sci. Rep. **11**, 7652 (2021).

[86] S. Sakamoto, G. Q. Zhao, G. Shibata, Z. Deng, K. Zhao, X. C. Wang, Y. Nonaka, K. Ikeda, Z. D. Chi, Y. X. Wan *et al.*, Anisotropic spin distribution and perpendicular magnetic anisotropy in a layered ferromagnetic semiconductor (Ba, K)$(Zn, Mn)_2As_2$, ACS Appl. Electron. Mater. **3**, 789 (2021).

[87] H. J. Zhang, R. F. Zhang, L. C. Fu, Y. L. Gu, G. X. Zhi, J. O. Dong, X. Q. Zhao, and F. L. Ning, $(La_{1-x}Sr_x)(Zn_{1-x}Mn_x)SbO$: A novel 1111-type diluted magnetic semiconductor, Acta Phys. Sinica **70**, 107501 (2021).

[88] G. Zhi, S. Guo, R. Zhang, Y. Zhao, L. Fu, Y. Gu, K. Wang, H. Zhang, X. Zhao, J. Dong *et al.*, $Cu_2(Zn, Mn)(Sn, Al)Se_4$: A diluted magnetic semiconductor with decoupled charge and spin doping, J. Magn. Magn. Mater. **536**, 168064 (2021).

[89] J. Dong, X. Zhao, L. Fu, Y. Gu, R. Zhang, Q. Yang, L. Xie, and F. Ning, (Ca, K)$(Zn, Mn)_2As_2$: Ferromagnetic semiconductor induced by decoupled charge and spin doping in $CaZn_2As_2$, J. Semicond. **43**, 072501 (2022).

[90] Y. Gu, R. Zhang, H. Zhang, L. Fu, G. Zhi, J. Dong, X. Zhao, L. Xie, and F. Ning, A $CaAl_2Si_2$-type magnetic semiconductor (Sr, Na)$(Zn, Mn)_2Sb_2$ isostructural to 122-type iron-based superconductors, Adv. Condens. Matter Phys. **2022**, 7 (2022).

[91] H. Suzuki, G. Zhao, J. Okamoto, S. Sakamoto, Z.-Y. Chen, Y. Nonaka, G. Shibata, K. Zhao, B. Chen, W.-B. Wu *et al.*, Magnetic properties and electronic configurations of Mn ions in the diluted magnetic semiconductor $Ba_{1-x}K_x(Zn_{1-y}Mn_y)_2As_2$ studied by x-ray magnetic circular dichroism and resonant inelastic x-ray scattering, J. Phys. Soc. Jpn. **91**, 064710 (2022).

[92] R. Zhang, C. Xu, L. Fu, Y. Gu, G. Zhi, J. Dong, X. Zhao, L. Xie, H. Zhang, C. Cao *et al.*, Manipulation of the ferromagnetic ordering in magnetic semiconductor (La,Ca)(Zn,Mn)AsO by chemical pressure, J. Magn. Magn. Mater. **554**, 169276 (2022).

[93] X. D. Zhao, J. Dong, L. Fu, Y. Gu, R. Zhang, Q. Yang, L. Xie, Y. Tang, and F. Ning, $(Ba_{1-x}Na_x)F(Zn_{1-x}Mn_x)Sb$: A novel fluoride-antimonide magnetic semiconductor with decoupled charge and spin doping, J. Semicond. **43**, 112501 (2022).

[94] Y. Peng, L. Shi, G. Zhao, J. Zhang, J. Zhao, X. Wang, Z. Deng, and C. Jin, Colossal magnetoresistance in layered diluted magnetic semiconductor Rb(Zn, Li, Mn)$_4As_3$ single crystals, Nanomaterials **14**, 263 (2024).

[95] Y. Peng, X. Li, L. Shi, G. Zhao, J. Zhang, J. Zhao, X. Wang, B. Gu, Z. Deng, Y. J. Uemura, and C. Jin, A near room temperature Curie temperature of 260 K in a new type of diluted magnetic semiconductor (Ba, K)$(Zn, Mn)_2As_2$, Adv. Phys. Res. **4**, 2570001 (2025).

[96] G. Zhao, Y. Cai, K. M. Kojima, Q. Sheng, J. Beare, G. Luke, X. Li, Y. Peng, T. Ziman, K. Zhao *et al.*, Magnetic evolution of carrier doping and spin dynamics in diluted magnetic semiconductors (Ba, Na)$(Zn, Mn)_2As_2$, Condens. Matter **10**, 30 (2025).

[97] X. Li, X. Wu, and J. Yang, Control of spin in a La(Mn,Zn)AsO alloy by carrier doping, J. Mater. Chem. C **1**, 7197 (2013).

[98] A. Djied, H. Khachai, T. Seddik, R. Khenata, A. Bouhemadou, N. Guechi, G. Murtaza, S. Bin-Omran, Z. A. Alahmed, and M. Ameri, Structural phase transition, mechanical and optoelectronic properties of the tetragonal NaZnp: *Ab-initio* study, Comput. Mater. Sci. **84**, 396 (2014).

[99] J. K. Glasbrenner and I. I. Mazin, First-principles evidence of Mn moment canting in hole-doped $Ba_{1-2x}K_{2x}Mn_2As_2$, Phys. Rev. B **89**, 060403 (2014).

[100] J. K. Glasbrenner, I. Žutić, and I. I. Mazin, Theory of Mn-doped II-II-V semiconductors, Phys. Rev. B **90**, 140403 (2014).

[101] I. R. Shein and A. L. Ivanovskii, Elastic, electronic properties and intra-atomic bonding in orthorhombic and tetragonal polymorphs of $BaZn_2As_2$ from first-principles calculations, J Alloy Compd **583**, 100 (2014).

[102] J. Deng, Z. Wu, W. Yang, Y.-T. Cui, A. Hu, R.-Y. Zhao, and W. MinDi, Electronic structures and optical properties of new diluted magnetic semiconductor Cu-doped LiMgN, Chin. Sci. Bull. **60**, 830 (2015).

[103] L. Hua and Q. L Zhu, The ferromagnetic origin of Mn-doped $Sr_3La_2O_5Zn_2As_2$: A first-principles study, Pis'ma v ZhETF **101**, 897 (2015).

[104] J. T. Yang, S. J. Luo, and Y. C. Xiong, First-principles study on the electronic structures and magnetic properties of a diluted magnetic semiconductor $(Ba_{1-x}K_x)(Zn_{1-y}Mn_y)_2As_2$, Solid State Sci. **46**, 102 (2015).

[105] B. Gu and S. Maekawa, Diluted magnetic semiconductors with narrow band gaps, Phys. Rev. B **94**, 155202 (2016).

[106] L. Hua, J. N. Zhu, and Z. T Lu, The ferromagnetic origin of Na and Mn co-doped $CaZn_2As_2$ diluted magnetic semiconductor: A first-principles study, Pis'ma v ZhET **103**, 715 (2016).

[107] J.-T. Yang, S.-J. Luo, and Y.-C. Xiong, Magnetic mechanism investigations on K and Mn co-doped diluted magnetic

semiconductor (Sr, K)(Zn, Mn)$_2$As$_2$, J. Magn. Magn. Mater. **407**, 334 (2016).

[108] S. M. Griffin and J. B. Neaton, Prediction of a new class of half-metallic ferromagnets from first principles, Phys. Rev. Mater. **1**, 044401 (2017).

[109] B. Gu and S. Maekawa, New p- and n-type ferromagnetic semiconductors: Cr-doped BaZn$_2$As$_2$, AIP Adv. **7**, 055805 (2017).

[110] Y. Cui, J. G. Zhu, H. L. Tao, S. M. Liu, Y. Z. Lv, M. He, B. Song, and Z. H. Zhang, Investigations on ferromagnetism of Li and Mn co-doped LiZnN by first-principles calculations, J. Am. Ceram. Soc. **102**, 303 (2018).

[111] H.-C. Yang, K. Liu, and Z.-Y. Lu, Magnetic interactions in a proposed diluted magnetic semiconductor ($Ba_{1-x}K_x$)($Zn_{1-y}Mn_y$)$_2$P$_2$, Chin. Phys. B **27**, 067103 (2018).

[112] A. Hirohata, H. Sukegawa, H. Yanagihara, I. Zutic, T. Seki, S. Mizukami, and R. Swaminathan, Roadmap for emerging materials for spintronic device applications, IEEE Trans. Magn. **51**, 1 (2015).

[113] I. Žutić and T. Zhou, Tailoring magnetism in semiconductors, Sci. China: Phys. Mech. Astron. **61**, 067031 (2018).

[114] G. Zhao, Z. Deng, and C. Jin, Advances in new generation diluted magnetic semiconductors with independent spin and charge doping, J. Semicond. **40**, 081505 (2019).

[115] Y. Singh, A. Ellern, and D. C. Johnston, Magnetic, transport, and thermal properties of single crystals of the layered arsenide BaMn$_2$As$_2$, Phys. Rev. B **79**, 094519 (2009).

[116] Y. Singh, M. A. Green, Q. Huang, A. Kreyssig, R. J. McQueeney, D. C. Johnston, and A. I. Goldman, Magnetic order in BaMn$_2$As$_2$ from neutron diffraction measurements, Phys. Rev. B **80**, 100403(R) (2009).

[117] M. Rotter, M. Tegel, and D. Johrendt, Superconductivity at 38 K in the iron arsenide ($Ba_{1-x}K_x$)Fe$_2$As$_2$, Phys. Rev. Lett. **101**, 107006 (2008).

[118] G. Liu, G. Wang, Y. Zhu, H. Zhang, G. Zhang, X. Wang, Y. Zhou, W. Zhang, H. Liu, L. Zhao *et al.*, Development of a vacuum ultraviolet laser-based angle-resolved photoemission system with a superhigh energy resolution better than 1 meV, Rev. Sci. Instrum. **79**, 023105 (2008).

[119] A. Suter and B. M. Wojek, Musrfit: A free platform-independent framework for μSR data analysis, Physics Procedia **30**, 69 (2012).

[120] P. E. Blöchl, Projector augmented-wave method, Phys. Rev. B **50**, 17953 (1994).

[121] G. Kresse and J. Furthmüller, Efficient iterative schemes for *ab initio* total-energy calculations using a plane-wave basis set, Phys. Rev. B **54**, 11169 (1996).

[122] J. P. Perdew, K. Burke, and M. Ernzerhof, Generalized gradient approximation made simple, Phys. Rev. Lett. **77**, 3865 (1996).

[123] S. L. Dudarev, G. A. Botton, S. Y. Savrasov, C. J. Humphreys, and A. P. Sutton, Electron-energy-loss spectra and the structural stability of nickel oxide: An LSDA+U study, Phys. Rev. B **57**, 1505 (1998).

[124] H. J. Monkhorst and J. D. Pack, Special points for Brillouin-zone integrations, Phys. Rev. B **13**, 5188 (1976).

[125] J.-C. Lian, H.-Y. Wu, W.-Q. Huang, W. Hu, and G.-F. Huang, Algorithm for generating irreducible site-occupancy configurations, Phys. Rev. B **102**, 134209 (2020).

[126] J.-C. Lian, Y. Si, T. Huang, W.-Q. Huang, W. Hu, and G.-F. Huang, Highly efficient tree search algorithm for irreducible site-occupancy configurations, Phys. Rev. B **105**, 014201 (2022).

[127] M. Imada, A. Fujimori, and Y. Tokura, Metal-insulator transitions, Rev. Mod. Phys. **70**, 1039 (1998).

[128] N. F. Mott, Metal-insulator transition, Rev. Mod. Phys. **40**, 677 (1968).

[129] Y. Tokura and Y. Tomioka, Colossal magnetoresistive manganites, J. Magn. Magn. Mater. **200**, 1 (1999).

[130] M. B. Salamon and M. Jaime, The physics of manganites: Structure and transport, Rev. Mod. Phys. **73**, 583 (2001).

[131] H. W. Lehmann, Semiconducting properties of ferromagnetic CdCr$_2$Se$_4$, Phys. Rev. **163**, 488 (1967).

[132] C. Lin, C. Yi, Y. Shi, L. Zhang, G. Zhang, J. Müller, and Y. Li, Spin correlations and colossal magnetoresistance in HgCr$_2$Se$_4$, Phys. Rev. B **94**, 224404 (2016).

[133] A. P. Ramirez and M. A. Subramanian, Large enhancement of magnetoresistance in Tl$_2$Mn$_2$O$_7$: Pyrochlore versus perovskite, Science **277**, 546 (1997).

[134] P. Majumdar and P. Littlewood, Magnetoresistance in Mn pyrochlore: Electrical transport in a low carrier density ferromagnet, Phys. Rev. Lett. **81**, 1314 (1998).

[135] J. Wu, J. W. Lynn, C. J. Glinka, J. Burley, H. Zheng, J. F. Mitchell, and C. Leighton, Intergranular giant magnetoresistance in a spontaneously phase separated perovskite oxide, Phys. Rev. Lett. **94**, 037201 (2005).

[136] J. Seo, C. De, H. Ha, J. E. Lee, S. Park, J. Park, Y. Skourski, E. S. Choi, B. Kim, G. Y. Cho *et al.*, Colossal angular magnetoresistance in ferrimagnetic nodal-line semiconductors, Nature (London) **599**, 576 (2021).

[137] X. Y. Liu, L. Riney, J. Guerra, W. Powers, J. S. Wang, J. K. Furdyna, and B. A. Assaf, Colossal negative magnetoresistance from hopping in insulating ferromagnetic semiconductors, J. Semicond. **43**, 112502 (2022).

[138] K. Ueda, T. Yu, M. Hirayama, R. Kurokawa, T. Nakajima, H. Saito, M. Kriener, M. Hoshino, D. Hashizume, T.-h. Arima *et al.*, Colossal negative magnetoresistance in field-induced Weyl semimetal of magnetic half-Heusler compound, Nat. Commun. **14**, 6339 (2023).

[139] F. Du, L. Yang, Z. Nie, N. Wu, Y. Li, S. Luo, Y. Chen, D. Su, M. Smidman, Y. Shi *et al.*, Consecutive topological phase transitions and colossal magnetoresistance in a magnetic topological semimetal, npj Quantum Mater. **7**, 65 (2022).

[140] R. Singha, K. J. Dalgaard, D. Marchenko, M. Krivenkov, E. D. L. Rienks, M. Jovanovic, S. M. L. Teicher, J. Hu, T. H. Salters, J. Lin *et al.*, Colossal magnetoresistance in the multiple wave vector charge density wave regime of an antiferromagnetic Dirac semimetal, Sci. Adv. **9**, eadh0145 (2023).

[141] Y. Tokura, Critical features of colossal magnetoresistive manganites, Rep. Prog. Phys. **69**, 797 (2006).

[142] J. M. D. Coey, M. Viret, and S. von Molnár, Mixed-valence manganites, Adv. Phys. **58**, 571 (2009).

[143] T. Penney, M. W. Shafer, and J. B. Torrance, Insulator-metal transition and long-range magnetic order in EuO, Phys. Rev. B **5**, 3669 (1972).

[144] L. H. Chen, S. Jin, T. H. Tiefel, R. Ramesh, and D. Schurig, Large magnetoresistance in La-Ca-Mn-O films, IEEE Trans. Magn. **31**, 3912 (1995).

[145] L. H. Chen, T. H. Tiefel, S. Jin, T. T. M. Palstra, R. Ramesh, and C. Kwon, Colossal magnetoresistance in La-Y-Ca-Mn-O films, IEEE Trans. Magn. **32**, 4692 (1996).

[146] W. J. de Haas, J. de Boer, and G. J. van dën Berg, The electrical resistance of gold, copper and lead at low temperatures, Physica **1**, 1115 (1934).

[147] J. Kondo, Resistance minimum in dilute magnetic alloys, Prog. Theor. Phys. **32**, 37 (1964).

[148] Y. Niimi, M. Kimata, Y. Omori, B. Gu, T. Ziman, S. Maekawa, A. Fert, and Y. Otani, Strong suppression of the spin Hall effect in the spin glass state, Phys. Rev. Lett. **115**, 196602 (2015).

[149] H. Taniguchi, M. Watanabe, T. Ibe, M. Tokuda, T. Arakawa, T. Taniguchi, B. Gu, T. Ziman, S. Maekawa, K. Kobayashi *et al.*, Spin treacle in a frustrated magnet observed with spin current, Phys. Rev. B **102**, 094405 (2020).

[150] M. A. Mayer, P. R. Stone, N. Miller, H. M. Smith, O. D. Dubon, E. E. Haller, K. M. Yu, W. Walukiewicz, X. Liu, and J. K. Furdyna, Electronic structure of $(Ga_{1-x}Mn_x)As$ analyzed according to hole-concentration-dependent measurements, Phys. Rev. B **81**, 045205 (2010).

[151] S. Zhou, L. Li, Y. Yuan, A. W. Rushforth, L. Chen, Y. Wang, R. Böttger, R. Heller, J. Zhao, K. W. Edmonds *et al.*, Precise tuning of the curie temperature of (Ga,Mn)As-based magnetic semiconductors by hole compensation: Support for valence-band ferromagnetism, Phys. Rev. B **94**, 075205 (2016).

[152] H. Ohno, Making nonmagnetic semiconductors ferromagnetic, Science **281**, 951 (1998).

[153] A. P. Wijnheijmer, X. Martí, V. Holý, M. Cukr, V. Novák, T. Jungwirth, and P. M. Koenraad, Scanning tunneling microscopy reveals LiMnAs is a room temperature antiferromagnetic semiconductor, Appl. Phys. Lett. **100**, 112107 (2012).

[154] A. Pandey, R. S. Dhaka, J. Lamsal, Y. Lee, V. K. Anand, A. Kreyssig, T. W. Heitmann, R. J. McQueeney, A. I. Goldman, B. N. Harmon *et al.*, $Ba_{1-x}K_xMn_2As_2$: An antiferromagnetic local-moment metal, Phys. Rev. Lett. **108**, 087005 (2012).

[155] J. K. Bao, H. Jiang, Y. L. Sun, W. H. Jiao, C. Y. Shen, H. J. Guo, Y. Chen, C. M. Feng, H. Q. Yuan, Z. A. Xu *et al.*, Weakly ferromagnetic metallic state in heavily doped $Ba_{1-x}K_xMn_2As_2$, Phys. Rev. B **85**, 144523 (2012).

[156] W. L. Zhang, P. Richard, A. van Roekeghem, S. M. Nie, N. Xu, P. Zhang, H. Miao, S. F. Wu, J. X. Yin, B. B. Fu *et al.*, Angle-resolved photoemission observation of Mn-pnictide hybridization and negligible band structure renormalization in $BaMn_2As_2$ and $BaMn_2Sb_2$, Phys. Rev. B **94**, 155155 (2016).

[157] K. Binder and A. P. Young, Spin glasses: Experimental facts, theoretical concepts, and open questions, Rev. Mod. Phys. **58**, 801 (1986).

[158] J. A. Mydosh, Spin glasses: Redux: An updated experimental/materials survey, Rep. Prog. Phys. **78**, 052501 (2015).

[159] A. DeMonvel and A. Bovier, Spin glasses: Statics and dynamics, in *Summer School, Paris 2007*, edited by A. B. DeMonvel and A. Bovier (Birkhäuser Basel, Basle, Switzerland, 2009), Vol. 62, pp. 1–278.

[160] P. W. Anderson, Localisation theory and the CuMn problem: Spin glasses, Mater. Res. Bull. **5**, 549 (1970).

[161] V. Cannella and J. A. Mydosh, Magnetic ordering in gold-iron alloys, Phys. Rev. B **6**, 4220 (1972).

[162] C. Lacroix, P. Mendels, and F. Mila, *Introduction to Frustrated Magnetism: Materials, Experiments, Theory* (Springer Berlin, Heidelberg, 2011).

[163] C. Nisoli, Frustration(s) and the ice rule: From natural materials to the deliberate design of exotic behaviors, in *Frustrated Materials and Ferroic Glasses*, edited by T. Lookman and X. Ren (Springer, Cham, Switzerland, 2018), pp. 57–99.

[164] E. Vincent, J. Hammann, and M. Ocio, Real spin glasses relax slowly in the shade of hierarchical trees, J. Stat. Phys. **135**, 1105 (2009).

[165] T. Yamazaki, Y. J. Uemura, M. Takigawa, and C. Y. Huang, Time correlation of random moments in spin-glass CuMn observed by zero-field muon spin relaxation, J. Magn. Magn. Mater. **15-18**, 407 (1980).

[166] Y. J. Uemura, K. Nishiyama, and T. Yamazaki, Dynamics of a spin-glass CuMn detected by zero-field and longitudinal-field μ^+, Physica B & C **107**, 317 (1981).

[167] Y. J. Uemura, K. Nishiyama, T. Yamazaki, and R. Nakai, Muon spin relaxation in a spin-glass CuMn observed in finite longitudinal magnetic-fields, Solid State Commun. **39**, 461 (1981).

[168] K. Emmerich, F. N. Gygax, A. Hintermann, H. Pinkvos, A. Schenck, C. Schwink, and W. Studer, μSR investigations of the spin glass transition in CuMn, J. Magn. Magn. Mater. **31-34**, 1361 (1983).

[169] Y. J. Uemura, T. Yamazaki, D. R. Harshman, M. Senba, J. H. Brewer, E. Ansaldo, and R. Keital, Zero-field μSR in a spin glass CuMn (1.1 at.%): Precise measurement of static and dynamic effects below T_g, Hyperfine Interact. **18**, 453 (1984).

[170] H. Pinkvos, F. N. Gygax, A. Hoffheinz, J. Menslage, E. Lippelt, A. Schenck, and C. Schwink, Homogeneous vs. Inhomogeneous spin freezing in pure and Au-doped CuMn, Hyperfine Interact. **31**, 363 (1986).

[171] H. Pinkvos, F. N. Gygax, E. Lippelt, R. Neuhaus, A. Schenck, C. Schwink, and A. J. van der Wal, On the spin freezing in CuMn, J. Magn. Magn. Mater. **54-57**, 119 (1986).

[172] H. Pinkvos, A. Kalk, and C. Schwink, Zero-field μSR measurements in CuMn and AuMn spin glasses interpreted in the frame of a fractal cluster model, Phys. Rev. B **41**, 590 (1990).

[173] A. Kalk, H. Pinkvos, C. Schwink, F. N. Gygax, and A. Schenck, Importance of the structural state of CuMn and AuMn for the spin freezing process—Susceptibility and μSR-studies, J. Magn. Magn. Mater. **102**, 184 (1991).

[174] Y. J. Uemura, T. Yamazaki, R. S. Hayano, R. Nakai, and C. Y. Huang, Zero-field spin relaxation of μ^+ as a probe of the spin dynamics of AuFe and CuMn spin-glasses, Phys. Rev. Lett. **45**, 583 (1980).

[175] Y. J. Uemura, T. Yamazaki, D. R. Harshman, M. Senba, and E. J. Ansaldo, Muon-spin relaxation in AuFe and CuMn spin glasses, Phys. Rev. B **31**, 546 (1985).

[176] J. A. Brown, R. H. Heffner, T. A. Kitchens, M. Leon, C. E. Olsen, M. E. Schillaci, S. A. Dodds, and D. E. MacLaughlin, Anomalous paramagnetic-state μSR in spin-glass AgMn, J. Appl. Phys. **52**, 1766 (1981).

[177] R. H. Heffner, M. Leon, M. E. Schillaci, D. E. MacLaughlin, and S. A. Dodds, Muon spin relaxation studies of the spin glass AgMn (invited), J. Appl. Phys. **53**, 2174 (1982).

[178] R. H. Heffner, M. Leon, M. E. Schillaci, D. E. MacLaughlin, and S. A. Dodds, Muon spin relaxation measurements of the fluctuation modes in spin-glass AgMn, J. Magn. Magn. Mater. **31-34**, 1363 (1983).

[179] D. E. MacLaughlin, L. C. Gupta, D. W. Cooke, R. H. Heffner, M. Leon, and M. E. Schillaci, Evidence for power-law spin-correlation decay from muon spin relaxation in AgMn spin-glass, Phys. Rev. Lett. **51**, 927 (1983).

[180] R. H. Heffner, D. W. Cooke, M. Leon, M. E. Schillaci, D. E. Maclaughlin, and L. C. Gupta, Muon spin relaxation measurements of spin-correlation decay in spin-glass AgMn, Hyperfine Interact. **18**, 463 (1984).

[181] R. H. Heffner, D. W. Cooke, R. L. Hutson, M. E. Schillaci, S. A. Dodds, G. A. Gist, and D. E. MacLaughlin, Muon spin relaxation study of exchange coupling in dilute AgMn alloys, J. Magn. Magn. Mater. **54-57**, 1103 (1986).

[182] Y. J. Uemura, A. Keren, K. Kojima, L. P. Le, G. M. Luke, W. D. Wu, Y. Ajiro, T. Asano, Y. Kuriyama, M. Mekata *et al.*, Spin fluctuations in frustrated kagome lattice system $SrCr_8Ga_4O_{19}$ studied by muon spin relaxation, Phys. Rev. Lett. **73**, 3306 (1994).

[183] A. Keren, L. P. Le, G. M. Luke, W. D. Wu, Y. J. Uemura, Y. Ajiro, T. Asano, H. Kuriyama, M. Mekata, and H. Kikuchi, Muon spin relaxation measurements in kagome lattice system $SrCr_8Ga_4O_{19}$, Hyperfine Interact. **85**, 181 (1994).

[184] S. R. Dunsiger, R. F. Kiefl, K. H. Chow, B. D. Gaulin, M. J. P. Gingras, J. E. Greedan, A. Keren, K. Kojima, G. M. Luke, W. A. MacFarlane *et al.*, Low temperature spin dynamics of geometrically frustrated antiferromagnets $Y_2Mo_2O_7$ and $Y_2Mo_{1.6}Ti_{0.4}O_7$ studied by muon spin relaxation, J. Appl. Phys. **79**, 6636 (1996).

[185] S. R. Dunsiger, R. F. Kiefl, K. H. Chow, B. D. Gaulin, M. J. P. Gingras, J. E. Greedan, A. Keren, K. Kojima, G. M. Luke, W. A. MacFarlane *et al.*, Muon spin relaxation investigation of the spin dynamics of geometrically frustrated antiferromagnets $Y_2Mo_2O_7$ and $Tb_2Mo_2O_7$, Phys. Rev. B **54**, 9019 (1996).

[186] S. R. Dunsiger, R. F. Kiefl, K. H. Chow, B. D. Gaulin, M. J. P. Gingras, J. E. Greedan, A. Keren, K. Kojima, G. M. Luke, W. A. MacFarlane *et al.*, Muon spin relaxation investigation of frustrated antiferromagnetic pyrochlores $A_2B_2O_7$, Hyperfine Interact. **104**, 275 (1997).

[187] B. A. Frandsen, L. Liu, S. C. Cheung, Z. Guguchia, R. Khasanov, E. Morenzoni, T. J. S. Munsie, A. M. Hallas, M. N. Wilson, Y. Cai *et al.*, Volume-wise destruction of the antiferromagnetic Mott insulating state through quantum tuning, Nat. Commun. **7**, 12519 (2016).

[188] A. Yaouanc and P. D. de Réotier, *Muon Spin Rotation, Relaxation, And Resonance: Applications To Condensed Matter* (Oxford University Press, Oxford, 2010), Vol. 147.

[189] P. Carretta and A. Lascialfari, *NMR-MRI, μSR and Mössbauer Spectroscopies in Molecular Magnets* (Springer Milano, Milan, Italy, 2007), p. 1.

[190] A. Amato and E. Morenzoni, *Introduction to Muon Spin Spectroscopy: Applications to Solid State and Material Sciences* (Springer, Cham, Switzerland, 2024).

[191] O. Hartmann, The positive muon as a probe in magnetism, Hyperfine Interact. **49**, 61 (1989).

[192] See Supplemental Material at http://link.aps.org/supplemental/10.1103/myxg-tt85 for comprehensive details regarding the μSR spectra and their analysis of the compounds Na(Zn,Mn)Sb, Li(Zn,Mn)As, Li(Zn,Mn)P, and Li(Zn,Cu,Mn)As under zero field, weak transverse field, and longitudinal field configurations.

[193] Z. Guguchia, B. A. Frandsen, D. Santos-Cottin, S. C. Cheung, Z. Gong, Q. Sheng, K. Yamakawa, A. M. Hallas, M. N. Wilson, Y. Cai *et al.*, Probing the quantum phase transition in mott insulator $BaCoS_2$ tuned by pressure and Ni substitution, Phys. Rev. Mater. **3**, 045001 (2019).

[194] B. A. Frandsen, Y. Kalcheim, I. Valmianski, A. S. McLeod, Z. Guguchia, S. C. Cheung, A. M. Hallas, M. N. Wilson, Y. Cai, G. M. Luke *et al.*, Intertwined magnetic, structural, and electronic transitions in V_2O_3, Phys. Rev. B **100**, 235136 (2019).

[195] W. Bronger, P. Mueller, R. Hoeppner, and H. U. Schuster, The magnetic properties of NaMnP, NaMnAs, NaMnSb, NaMnBi, LiMnAs, and KMnAs, characterized by neutron diffraction experiments, Z. Anorg. Allg. Chem. **539**, 175 (1986).

[196] B. I. Yoo, N. Lee, B. Lamichhane, J. Bang, H. Y. Song, B. C. Park, K. H. Lee, S.-G. Kim, and S. W. Kim, Identifying the correlation between structural parameters and anisotropic magnetic properties in I-Mn-V semiconductors: A possible room-temperature magnetism, Adv. Mater. **34**, 2200074 (2022).

[197] R. Bouzerar, G. Bouzerar, and T. Ziman, Why RKKY exchange integrals are inappropriate to describe ferromagnetism in diluted magnetic semiconductors, Phys. Rev. B **73**, 024411 (2006).

[198] G. Bouzerar, T. Ziman, and J. Kudrnovsky, Compensation, interstitial defects, and ferromagnetism in diluted ferromagnetic semiconductors, Phys. Rev. B **72**, 125207 (2005).

[199] P. Nemec, V. Novak, N. Tesarova, E. Rozkotova, H. Reichlova, D. Butkovicova, F. Trojanek, K. Olejnik, P. Maly, R. P. Campion *et al.*, The essential role of carefully optimized synthesis for elucidating intrinsic material properties of (Ga,Mn)As, Nat. Commun. **4**, 1422 (2013).

[200] X. Li, J.-W. Li, J.-Y. You, G. Su, and B. Gu, High curie temperature in diluted magnetic semiconductors (B, Mn)X (X = N, P, As, Sb), Phys. Rev. B **111**, 184425 (2025).

[201] R. Bacewicz and T. F. Ciszek, Preparation and characterization of some $A^{\mathrm{I}}B^{\mathrm{II}}C^{\mathrm{V}}$ type semiconductors, Appl. Phys. Lett. **52**, 1150 (1988).

[202] T. Jungwirth, V. Novák, X. Martí, M. Cukr, F. Máca, A. B. Shick, J. Mašek, P. Horodyská, P. Němec, V. Holý *et al.*, Demonstration of molecular beam epitaxy and a semiconducting band structure for I-Mn-V compounds, Phys. Rev. B **83**, 035321 (2011).

[203] J. Yang, A. Wegner, C. M. Brown, and D. Louca, Defect-driven extreme magnetoresistance in an I-Mn-V semiconductor, Appl. Phys. Lett. **113**, 122105 (2018).

[204] K. Kuriyama, T. Kato, and K. Kawada, Optical band gap of the filled tetrahedral semiconductor LiZnAs, Phys Rev B **49**, 11452 (1994).

[205] K. Kuriyama and F. Nakamura, Electrical transport properties and crystal structure of LiZnAs, Phys. Rev. B **36**, 4439 (1987).

[206] A.-L. Wang, Z.-M. Wu, C. Wang, A.-Y. Hu, and R.-Y. Zhao, First-priciples study on Mn-doped LiZnAs, a new diluted magnetic semiconductor, Acta Phys. Sin. **62**, 137101 (2013).

[207] M. Wang, Z. Zhang, M. He, H. Tao, T. Yang, B. Song, and L. Lin, Investigations on magnetic properties of Cr-doped

LiZnAs by first-principle calculations, J. Supercond. Novel Magn. **30**, 1545 (2017).

[208] A. Beleanu, J. Kiss, G. Kreiner, C. Köhler, L. Müchler, W. Schnelle, U. Burkhardt, S. Chadov, S. Medvediev, D. Ebke *et al.*, Large resistivity change and phase transition in the antiferromagnetic semiconductors LiMnAs and LaOMnAs, Phys. Rev. B **88**, 184429 (2013).

[209] K. Kuriyama, T. Katoh, and N. Mineo, Crystal growth and characterization of the filled tetrahedral semiconductor LiZnP, J. Cryst. Growth **108**, 37 (1991).

[210] U. Chopra, M. Zeeshan, S. Pandey, R. Dhawan, H. K. Singh, J. van den Brink, and H. C. Kandpal, First-principles study of thermoelectric properties of Li-based Nowotony–Juza phases, J. Phys.: Condens. Matter **31**, 505504 (2019).

[211] J. S. Blakemore, Semiconducting and other major properties of gallium arsenide, J. Appl. Phys. **53**, R123 (1982).

[212] S. Haneda, N. Kazama, Y. Yamaguchi, and H. Watanabe, Electronic state of high spin MnAs, J. Phys. Soc. Jpn. **42**, 1201 (1977).

[213] B. Saparov, J. E. Mitchell, and A. S. Sefat, Properties of binary transition-metal arsenides (*T*As), Supercond. Sci. Technol. **25**, 084016 (2012).

[214] Y. Issa Diakite, S. D. Traore, Y. Malozovsky, B. Khamala, L. Franklin, and D. Bagayoko, Accurate electronic, transport, and bulk properties of gallium arsenide (GaAs), arXiv:1601.05300v1.

[215] Q. Sheng, T. Kaneko, K. Yamakawa, Z. Guguchia, Z. Gong, G. Zhao, G. Dai, C. Jin, S. Guo, L. Fu *et al.*, Two-step Mott transition in $Ni(S, Se)_2$: μSR studies and charge-spin percolation model, Phys. Rev. Res. **4**, 033172 (2022).

[216] C. Xu, C. Zhang, M. Wang, Y. Xie, R. Hübner, R. Heller, Y. Yuan, M. Helm, X. Zhang, and S. Zhou, *P*-type codoping effect in (Ga,Mn)As: Mn lattice location versus magnetic properties, Phys. Rev. Mater. **3**, 084604 (2019).